MICROGLIA AGING IN THE HIPPOCAMPUS ADVANCES THROUGH INTERMEDIATE STATES THAT DRIVE ACTIVATION AND COGNITIVE DECLINE

Jeremy M. Shea[1]# and Saul A. Villeda[1-3]#

1. Department of Anatomy, University of California San Francisco, San Francisco, California 94143, USA
2. Department of Physical Therapy and Rehabilitation Science, University of California San Francisco, San Francisco, California 94143, USA
3. Bakar Aging Research Institute, University of California San Francisco, San Francisco, California, 94143, USA

#Corresponding Authors:

Dr. Saul Villeda, PhD
University of California San Francisco
Department of Anatomy
513 Parnassus Ave, Box 0452
San Francisco, CA 94143
Email: saul.villeda@ucsf.edu
Tel: 415-502-1929

Dr. Jeremy Shea, PhD
University of California San Francisco
Department of Anatomy
513 Parnassus Ave, Box 0452
San Francisco, CA 94143
Email: jeremy.shea@ucsf.edu
Tel: 617-460-4122

SUMMARY

During aging, microglia – the resident macrophages of the brain – exhibit altered phenotypes and contribute to age-related neuroinflammation. While numerous hallmarks of age-related microglia have been elucidated, the progression from homeostasis to dysfunction during the aging process remains unresolved. To bridge this gap in knowledge, we undertook complementary cellular and molecular analyses of microglia in the mouse hippocampus across the adult lifespan and in the experimental aging model of heterochronic parabiosis. Single-cell RNA-Seq and pseudotime analysis revealed age-related transcriptional heterogeneity in hippocampal microglia and identified intermediate states of microglial aging that also emerge following heterochronic parabiosis. We tested the functionality of intermediate stress response states via TGFβ1 and translational states using pharmacological approaches *in vitro* to reveal their modulation of the progression to an activated state. Furthermore, we utilized single-cell RNA-Seq in conjunction with *in vivo* adult microglia-specific *Tgfb1* conditional genetic knockout mouse models, to demonstrate that microglia advancement through intermediate aging states drives transcriptional inflammatory activation and hippocampal-dependent cognitive decline.

INTRODUCTION

Microglia are one of few immune cells with long term residence in the brain parenchyma[1]. Microglia support neural development by synaptic pruning and neurogenic function in the developing brain, followed by homeostatic maintenance in the adult brain[2]. Alternatively, in the aged brain microglia exhibit unbalanced phenotypes, aggravating perceived insults rather than responding productively to environmental signals[3]. While microglia have been identified as principal mediators of multiple age-related neurodegenerative pathologies[4], mechanisms leading to microglia dysfunction during aging remain obscure.

Numerous studies have indicated that aged microglia are inflamed[5], have reduced phagocytic capacity[6,7], and have decreased motility[8]. Microglia exhibit several hallmarks of aging that potentially contribute to their age-related dysfunction, such as shortened telomeres[9], altered intercellular communication[10], molecular alterations[11], and a loss of proteostasis[12]. Furthermore, many recent studies have started to reveal the molecular changes that define microglial aging. Single cell RNA-Seq (scRNA-Seq) analyses indicate that microglia isolated from the entire brain lose homeostasis and activate inflammatory transcriptional profiles with age[13,14]. Data rich studies have also revealed partial overlaps between aging microglia and those from disease models, including Alzheimer's disease[15-19]. Interestingly, the microglial response to aging shows regional variation, as white matter-rich regions induce an interferon signature in aged microglia[20]. Studies using aged plasma administration and heterochronic blood exchange demonstrate that microglia aging is in part driven by the aged systemic environment [21,22]. However, the genesis of age-related microglial phenotypes has not been extensively investigated. So, we set out to characterize the progression of age-related hippocampal microglial changes, aiming to uncover intermediate states that could be intrinsic to the aging process. To do so, we undertook complementary cellular and molecular analyses of microglia across the adult lifespan and in heterochronic parabiosis - an experimental model of aging in which the circulatory systems of young adult and aged animals are joined[23].

In this study, we report that microglia in the adult mouse hippocampus, a brain region responsible for learning and memory and susceptible to age-related cognitive decline, advance through intermediate states that drive inflammatory activation during aging. We utilize scRNA-Seq across the adult lifespan to identify intermediate transcriptional states of microglial aging that emerge following exposure to an aged systemic environment. We observe heterogeneous spatiotemporal dynamics of microglia activation across the adult lifespan with pseudotime and immunohistochemical analysis. Functionally, we tested the role of these intermediate states using *in vitro* microglia approaches and *in vivo* temporally controlled adult microglia-specific *Tgfb1*

conditional genetic knockout mouse models to demonstrate that intermediates represent modulators of the progression of microglia from homeostasis to activation, with functional implications for hippocampal-dependent cognitive decline.

RESULTS

Complementary single-cell transcriptional and immunohistochemical analysis reveals the dynamics of heterogeneous hippocampal microglia aging

Previously, single-cell transcriptional profiling of microglia uncovered a diversity of responses during development and in response to pathology aggregated over multiple brain regions[13,14,16,19,24,25]. Microglia have region-specific transcriptional states, so we decided to focus our analyses on the hippocampus[11], a region with well-reported functional differences during aging[26]. Correspondingly, we investigated age-related transcriptional heterogeneity by performing scRNA-Seq on hippocampal CD11b-positive cells isolated from mice across numerous life stages at mature (6 months), middle-age (12 months), aged (18 months), and old age (24 months) using a commonly employed pooling strategy[18,27,28] (n = 1 pool of 5 biological replicates for each age) to reveal the dynamics of microglia aging. 82% of cells isolated with CD11b were identified as microglia using canonical markers with a small subset being proliferative (Figure S1A-C). Dimensionality reduction revealed that non-proliferative microglia were grouped into interconnected clusters that contained homeostatic, transition, and activated states, along with a semi-distinct cluster with interferon activation (Figure 1a, S1D-G). Overlaying microglia ages onto the clusters revealed progression from a homeostatic state in younger microglia to an activated state in old microglia, suggesting that gradual transcriptional changes occur during microglial aging (Figure 1B,C, S1H). Furthermore, the heterogeneity of microglial transcriptional programs increased with age (Figure S1I). Expression of *Cx3cr1* and *Itgam* exemplified the homeostatic state, while *B2m*, *Apoe*, *Cd48*, and *Lyz2* depict the activated state (Figure 1D). Interestingly, several immediate early genes (*Jun*, *Klf2*, *Fos*), as well as the purinergic receptor gene *P2ry12*, exhibited transient increases in expression at middle-age (Figure 1D). Alternatively, the interferon cluster represents a small proportion of the overall microglia population with little age-related changes in the number of these cells, but augmented expression of interferon genes during aging (Figure 1A,C,D, S1G). Thus, gene expression changes exhibited unique patterns during aging, with certain genes showing age-related decreases (e.g. *Tgfbr1*) or increases (e.g. *Apoe*), while a subset of genes (e.g. *Tgfb1*) have peaks of expression at middle age (Figure 1D,E,G; Table S1). Several complement genes implicated in age-related synaptic loss[10,29](e.g. *C1q* and *C3*)

152 demonstrated progressive age-related transcriptional increases, and the increased complement
153 activity in microglia was confirmed by immunohistochemistry (Figure 1E,F).
154 The effects of aging on microglia could be progressive or sudden, so we investigated if we
155 could find evidence of early aging of hippocampal microglia. We observe relatively few
156 differentially genes between 6- and 12-month (Figure 1G,H, Table S1). The number of
157 differentially expressed genes gradually increased through the 24-month time point (Figure 1G-J,
158 Table S1), suggesting that hippocampal microglia progressively accumulate aged-related
159 expression changes. Furthermore, when investigating the outcome for genes with significant
160 changes for each age, we find that genes that are differentially expressed at 12 months lose their
161 expression change, while genes that change at later ages show progressive expression
162 differences (Figure 1H). GO analysis of the microglia from 6- and 12-month-old mice revealed
163 that activation and translational programs are modestly enriched in genes with increased
164 expression during early aging (Figure 1I). The latter stages of aging display more prominent
165 enrichment of immune activation and translation processes in genes with increased expression,
166 while revealing that genes that regulate transcriptional processes exhibit decreased expression
167 (Figure 1J,K). Thus, microglia progressively age with subsets of cells at each age group being
168 forerunners towards inflammatory activation or refractory to aging by remaining homeostatic. This
169 analysis further suggests that microglia could pass through transitory states during aging.
170 As scRNA-Seq analysis revealed transcriptional heterogeneity during hippocampal
171 microglial aging, we next assessed microglial phenotypic diversity across hippocampal
172 subregions that could mirror the differential impact of aging across these hippocampal subregions
173 at a functional level[30,31]. We subdivided the adult hippocampus into functional units, and quantified
174 accumulation of puncta of the lysosomal marker CD68 in microglia to identify activation in the
175 dentate gyrus (DG), molecular layer (ML), granule cell layer (GC), hilus, CA3, and CA1 at 3, 6,
176 12, 18, and 24 months of age (Figure S2A-C). We find striking spatial differences in microglial
177 activation patterns during aging, with the GC, hilus, CA3, and outer CA1 regions showing robust
178 microglia activation that increases beginning at middle age, while the ML and inner CA1 exhibit
179 no age-related activation (Figure S2D-F). Additionally, we characterized the levels of the pro-
180 inflammatory transcription factor NFKB p65 in microglia during aging[32]. Microglia-specific
181 expression of NFKB p65 demonstrates region- and age-specific accumulation that mirrors, in part,
182 age-related microglial CD68 increase (Figure S2G-I). These results indicate temporally defined
183 and spatially heterogeneous microglia activation within the aging hippocampus that complements
184 the identification of heterogeneous transcriptional activation of microglia during aging.
185

186 **Trajectory analysis indicates that aging microglia pass through intermediate states**
187 To determine the transcriptional progression of microglia aging towards an activated state, we
188 performed pseudotime analysis of the scRNA-Seq data using Monocle and observed several
189 trajectories (Figure 2A). We find that the pseudotime trajectories progressed along the biological
190 ages of the mice, indicating the suitability of this analysis for modeling aging progression in
191 microglia (Figure 2B). We focus our analysis on one trajectory with two semi-distinct subbranches
192 that terminated in transcriptional inflammatory activation, since the alternate branch had minimal
193 transcriptional differences between the beginning and end of the trajectory (Figure 2B,C). To gain
194 insight into the transcriptional states of microglial aging along this inflammatory trajectory, we
195 used spatial autocorrelation analysis and identified five expression modules of coregulated genes
196 (Figure 2B,C, Table S2). We named these modules according to the most enriched GO pathways
197 and known roles of prominent genes for microglia. This trajectory proceeds from high expression
198 of homeostatic genes and mitochondrial processes (module 1) to transient expression of stress
199 response genes and *Tgfb1* (module 2), of which TGFβ signaling is critical for microglia
200 development[33,34]. A concerted increase in expression of ribosomal genes (module 3) precedes
201 one subbranch of inflammatory activation (module 4), while the other myeloid activation
202 subbranch (module 5), characterized by *B2m* and *C1qc* expression, proceeds independently of
203 increased ribosomal gene expression. GO analysis of genes specifically upregulated at 12-
204 months showed an enrichment of stress response pathways (Figure S3A,B), corroborating the
205 findings of the pseudotime analysis that intermediate stages of microglial aging pass through
206 stress response pathways. We complemented Monocle pseudotime analysis using another
207 distinct trajectory analysis (Scorpius) that uncovered similar progression through stress-response
208 and translational intermediate states, followed by inflammatory activation (Figure S3C-D). We
209 further corroborate the transient nature of the intermediate stress response module (module 2),
210 observing KLF2 expression that peaks at 18 months of age by immunohistochemistry (Figure 2H)
211 and *Tgfb1* expression that has a transient peak at 12 months of age by RNAscope (Figure 3B).
212 Thus, pseudotime trajectory analysis identifies a progression of intermediate states of microglial
213 aging.
214 The gene level dynamics of microglia aging are further revealed when interrogating the
215 modules at each timepoint. Expression of several genes in the homeostatic cluster, including
216 *Cx3cr1* and *Tgfbr1*, progressively decline throughout the aging timeline (Figure 2D). Stress
217 response gene expression peaks at early timepoints during aging, while those genes in the
218 translation module have coherent upregulation at 24-months of age (Figure 2D). The top ranked
219 genes in the inflammation module gradually increase their expression throughout aging in a

220 consistent manner (Figure 2D). Alternatively, several genes in the myeloid activation module have
221 expression peaks at 12- (*Cst3*, *Selplg*) *or* 18-months (*Ctss*, *Cd9*) of age (Figure 2D). When the
222 modules are collapsed into metagenes, we observe that the homeostatic module is reduced early
223 on in aging, while the stress response module follows later (Figure 2E-G). The ribosomal and
224 inflammatory modules display augmented expression at latter ages (Figure 2E-G). Alternatively,
225 the myeloid activation consistently has slightly increased expression throughout aging. These
226 results suggest that with advancing age microglia lose homeostatic and stress response
227 functions, while increasing their translational and inflammatory capacity.
228 Next, we used models of pro-aging systemic interventions[35] and age-related
229 neurodegenerative disease[36] to determine their impact on hippocampal microglia aging
230 trajectories. First, we used the heterochronic parabiosis model[37] to investigate whether exposure
231 to an aged systemic environment could promote progression of young adult microglia along the
232 identified aging trajectory (Figure 2I). Performing immunohistochemistry for IBA1 and CD68, we
233 reveal that an aged systemic environment activates microglia (Figure 2J). Next, we utilized
234 publicly available scRNA-Seq datasets of parabiosis[38] and Alzheimer's Disease[17] models to
235 investigate the transcription consequences of these interventions on microglia aging trajectories.
236 Analyzing the scRNA-Seq dataset from Palovics *et al*[38] we find that hippocampal microglia from
237 young adult heterochronic parabionts have decreased expression of homeostatic genes (module
238 1), while having increased expression of ribosomal genes (modules 3), inflammatory activation
239 genes (module 4) and myeloid activation genes (module 5) (Figure 2K, S3E). Using scRNA-Seq
240 from Sala Frigerio *et al*, we analyzed the $App^{NL\text{-}G\text{-}F}$ transgenic mouse model data at 12 months of
241 age to determine the effects of Alzheimer's disease pathology on microglial aging[17] (Figure 2L).
242 We observe exaggerated advancement along the aging trajectory in $App^{NL\text{-}G\text{-}F}$ mice compared to
243 controls, as expression is shifted towards the age-associated modules (Figure 2M, S3F,G). These
244 shifts in gene expression posit that the aged systemic and diseased environments drive adult
245 microglia advancement along an aging-associated transcriptional trajectory.
246
247 **Intermediate states of microglia aging act as modulators of age-related trajectory**
248 **progression**
249 Next, we sought to further corroborate microglial age-related molecular changes associated with
250 individual intermediate states in the aging hippocampus. Specifically, we assessed changes in
251 the intermediate stress response (module 2) and translation (module 3) modules by examining
252 expression of *Tgfb1* (Figure 3A,B) and the ribosomal protein S6 (Figure 3G,H), respectively. The
253 vast majority (>95%) of *Tgfb1* signal localized to microglia at every age (Figure S4A), indicating

254 microglia are the predominant source for hippocampal TGFB1. Consistent with scRNA-Seq
255 analysis (module 2) (Figure 1E), we observed highest *Tgfb1* expression in microglia by middle-
256 age using RNAscope (Figure 3B). TGFBR1 activation was reduced during aging in hippocampal
257 microglia (Figure S4B), and genes involved in the TGFβ signaling pathway exhibited age-related
258 expression changes with several having peak expression at 12 months of age (Figure 2C, S4C).
259 Next, we examined at a transcriptional level whether TGFβ1 is likely to act in an autocrine or
260 paracrine fashion in microglia. To do so, we interrogated our scRNA-Seq dataset, leveraging the
261 variation in microglia *Tgfb1* expression to probe the relative activity of TGFβ1. High expression of
262 downstream TGFβ signaling pathway components in microglia with high *Tgfb1* expression would
263 point to autocrine mechanisms while, alternatively, high expression of downstream TGFβ
264 signaling pathway components in microglia with low *Tgfb1* expression would point to paracrine
265 mechanisms. We observed highest expression of TGFβ signaling pathway components and
266 targets in microglia with the highest expression of *Tgfb1* (Figure S4E-G), suggesting an autocrine
267 mechanism of action. Additionally, consistent with an increase in translational components found
268 during the scRNA-Seq analysis (module 3), we observed increased expression of ribosomal
269 protein S6 (Figure 3I)[39] by immunohistochemistry.

270 To complement hippocampal aging analysis, we assessed the impact of the aging
271 systemic milieu on both the TGFβ pathway (module 2) and translational components (module 3)
272 in the young adult hippocampus following heterochronic parabiosis. Using the dataset from
273 Palovics *et al*[38], we observed a decrease in microglia *Tgfb1* and TGFβ pathway expression in
274 young adult heterochronic parabionts compared to age-matched young adult isochronic controls
275 (Figure 3C, S4D). Additionally, expression of the translation module in microglia increased
276 following exposure to an aged systemic environment in the heterochronic parabiosis model
277 (Figure 3J).

278 To investigate the role of the intermediate stress response (module 2) and translation
279 (module 3) modules in mediating advancement through microglial activation states, we used an
280 *in vitro* approach. Primary microglia were treated with LPS, which induced gene expression
281 changes with a significant overlap to aging, as well as expression changes in aging modules
282 genes (Figure S4H,I; Table S3). We administered TGFB1 to activate TGFβ signaling (module 2)
283 (Figure 3A) and CX-5461 to inhibit RNA Pol I synthesis and interfere with translation (module 3)
284 (Figure 3H) in the context of microglial activation. TGFB1 treatment modified the transcriptional
285 states of LPS-treated microglia (Figure S4J) and caused decreased expression of genes in GO
286 terms related to inflammatory immune processes after LPS stimulation (Figure 3E). TGFB1

287 treatment reduced expression of later aging modules (modules 2, 3 and 4) and restored
288 expression of the homeostatic gene *Cx3cr1* (Figure 3F,G), suggesting that TGFBβ signaling acts
289 as an aging modulator during microglial stress response. Targeting translation (module 3) with
290 CX-5461 attenuated expression of genes in GO terms related to immune processes after LPS
291 stimulation (Figure 3K; Table S3), as well as decreased expression of genes in modules 2, 3, and
292 4, while restoring expression of homeostatic genes in module 1 (Figure 3L,M). Interestingly, CX-
293 5461 treatment had no effect on genes in module 5, which is located on an independent myeloid
294 activation trajectory from altered translational gene expression (Figure 3L,M). These *in vitro*
295 perturbation data identify active roles for intermediate states in mediating advancement along
296 aging-associated inflammatory trajectories.
297

298 **Mimicking age-related changes in microglia-derived TGFB1 promotes microglial**
299 **advancement along an aging-associated inflammatory trajectory *in vivo***

300 Having uncovered roles for intermediate states in advancing microglia along aging-associated
301 trajectories *in vitro*, we next investigated the role of individual aging modules in adult microglia *in*
302 *vivo*. We elected to disrupt the transition from homeostasis to inflammatory activation by targeting
303 microglia-derived TGFB1, a key marker of the stress response intermediate state (module 2).
304 While TGFB1 is critical for microglia development[34,40], the role of microglia-derived TGFB1 in
305 regulating microglia homeostasis during aging remains to be defined.
306 We generated *Tgfb1*$^{flox/flox}$, *Tgfb1*$^{flox/wt}$, and *Tgfb1*$^{wt/wt}$ mice carrying an inducible *Cx3cr1-*
307 *Cre-ER* gene, in which *Tgfb1* is excised specifically in mature (7-8 months) microglia upon
308 tamoxifen administration (*Tgfb1* cKO, *Tgfb1* Het, and WT, respectively) (Figure 4A). To disrupt
309 the age-related increase in microglia *Tgfb1* observed between mature and middle-age (Figure 1E
310 and Figure 3B), mature mice were administered tamoxifen and molecular changes were assessed
311 two months later (Figure 4A). We find that microglia activation, as measured by CD68/IBA1
312 immunohistochemistry, exhibited genotype-dependent effects (Figure S5A). We performed
313 scRNA-Seq on microglia isolated from WT, *Tgfb1* Het and *Tgfb1* cKO mature mice (n = 2 pools
314 of 3 animals per genotype), and detected genotype-dependent changes in *Tgfb1*expression
315 levels, as well as effectors of TGFB1 signaling (Figure S5B). Dimensionality reduction and
316 clustering of cells from scRNA-Seq revealed readily identifiable clusters based on marker
317 expression (Figure 4B). Composition of these clusters were dependent on the microglia genotype,
318 with WT microglia representing the largest fraction of the homeostatic cluster and *Tgfb1* cKO
319 microglia representing the largest fraction of the activated cluster (Figure 4C, S5C). Next, we
320 assessed whether deletion of *Tgfb1* in mature adult microglia impacted advancement along aging-

321 associated inflammatory trajectories. Interestingly, when we analyze the effects of *Tgfb1* dosage
322 on the aging modules, we find that the loss of a single *Tgfb1* allele reduces expression of
323 homeostatic genes (module 1), while increasing expression of translation-related genes (module
324 3) (Figure 4D,E). In addition to a decrease in expression of homeostatic genes (module 1), loss
325 of both *Tgfb1* alleles caused a greater increase in expression of translation-related genes (module
326 3), and led to a profound increase in inflammatory activation genes (module 4) (Figure 4D,F).
327 Results were corroborated in an independent cohort of mature *Tgfb1* cKO mice, in which we
328 detected altered levels of immune- and age-related cell surface markers (Figure S5D,E),
329 transcriptional alterations that significantly overlapped with aging (Figure S5F-H; Table S4), and
330 progression along the aging-associated inflammatory trajectories (Figure S5I,J). These data
331 indicate that microglia-derived TGFB1 is both necessary for expression of youth-associated
332 homeostatic genes and prevents aberrant microglia inflammatory activation, further suggesting
333 that TGFBβ signaling acts as a modulator in mediating advancement along aging-associated
334 inflammatory trajectories.
335
336 **Mimicking age-related changes in microglia-derived TGFB1 impairs hippocampal-**
337 **dependent cognitive function**
338 It is becoming increasingly apparent that microglia interact with other cell types in the brain to
339 influence cognitive function[2,41]. Given that manipulating the levels of microglia-derived TGFB1
340 altered microglia homeostasis and progression along aging-associated trajectories, we next
341 investigated the functional consequence of the loss of microglia-derived TGFB1 on cognition. We
342 assessed hippocampal-dependent learning and memory in WT, *Tgfb1* Het and *Tgfb1* cKO mature
343 mice using novel object recognition and contextual fear conditioning - behavioral paradigms that
344 are sensitive to age-related impairments[42,43]. During novel object recognition testing, WT mature
345 mice were biased toward a novel object relative to a familiar object while neither *Tgfb1* Het or
346 *Tgfb1* cKO mature mice showed any preference (Figure 4G). During contextual fear conditioning
347 testing, *Tgfb1* Het and *Tgfb1* cKO mature mice exhibited less freezing compared to WT controls
348 (Figure 4H). Alternatively, we assessed amygdala-dependent fear memory by cued fear
349 conditioning (Figure S6A)[44] and short-term spatial reference memory by Y maze (Figure S6B)[45],
350 and observed no differences across genotypes. As a control, we also profiled general health using
351 an open field paradigm and observed no differences in total distance traveled or time spent in the
352 center of the open field, indicative of normal motor and anxiety functions (Figure S6C).
353 To further examine the age-dependent role of microglia-derived TGFB1 in cognitive
354 function, and complement our genetic approach, we utilized an alternative inducible microglia-

355 specific *Tmem119*-CreER mouse model[46] to manipulate *Tgfb1* expression at both young (2-3
356 month) and mature (7-8 month) ages (Figure 4I). We assessed hippocampal-dependent learning
357 and memory in WT, *Tgfb1* Het and *Tgfb1* cKO young and mature mice using novel object
358 recognition. During testing, young mice were biased toward a novel object relative to a familiar
359 object regardless of genotype (Figure 4J), indicating normal cognitive function despite loss of
360 microglia-specific *Tgfb1* at young age. However, while WT mature mice were biased toward a
361 novel object relative to a familiar object, both *Tgfb1* Het or *Tgfb1* cKO mature mice lost their
362 preference for the novel object (Figure 4K), indicating an age-dependent role for microglia-specific
363 *Tgfb1* in maintaining cognitive function. No differences were observed in either Y maze (Figure
364 S6D,F) or open field (Figure S6E,G) between genotypes at either young or mature ages. These
365 behavioral data indicate that loss of microglia-derived TGFB1 not only impacts aging-associated
366 trajectories but also promotes hippocampal-dependent cognitive impairments characteristic of
367 age-related functional decline in an age-dependent manner.
368
369 **DISCUSSION**
370 Cumulatively, we demonstrate that microglia aging in the hippocampus advances through
371 intermediate states that precede inflammatory activation, with functional implications for age-
372 related cognitive decline. These transient states, such as activation of the stress response and
373 TGFβ signaling, act as modulators of further age-related activation. Microglia demonstrate
374 spatiotemporal dissimilarities in advancement along aging trajectories across the hippocampus.
375 Furthermore, microglia progression through this aging trajectory is in turn influenced by the
376 systemic environment and neurodegenerative disease states.
377 Analysis of our scRNA-Seq data elucidate cryptic, but necessary, intermediate states of
378 microglia progression to age-related inflammatory activation. These states are present in middle-
379 aged mice and constitute stress response pathways likely responsive to internal and external
380 cellular insults[47,48]. Pseudotime analysis suggests a highly plausible sequence of molecular
381 alterations that lead to age-related inflammatory activation of hippocampal microglia. First,
382 mitochondrial dysfunction triggers a stress response, and products of this stress response (e.g.
383 TGFB1) attempt to return microglia to homeostasis[49]. Here, chronic activation of the stress
384 response leads to subsequent increased translational capacity that promotes inflammatory
385 activation[50]. Alternatively, another branch of microglial activation advances independently of
386 increased translational capacity, evidenced by translational inhibition having little effect on its
387 activation following LPS stimulation. Thus, we find that increases in translational capacity
388 predicate age-related inflammatory phenotypes, identifying potential targets to counter microglial

389 aging. Analysis of scRNA-Seq data further identify intermediate states of microglial aging in young
390 adult heterochronic parabionts, suggesting a pivotal role for the aged systemic environment in
391 driving advancement towards age-related inflammatory activation.

392 While we find evidence of the beginnings of inflammatory activation in the hippocampus
393 by middle age (12 months), consistent with the timing recently reported in the whole brain[14], it
394 should be noted that scRNA-Seq analysis of the whole brain did not observe intermediate stages
395 in microglial aging[14]. These disparate observations could likely be the result of analyzing multiple
396 regions with highly differentiated transcriptional programs[11] that could obfuscate regional aging
397 trajectories. This further underscores the need for both temporal and regional specificity in aging
398 studies, given the level of cellular heterogeneity observed across ages and brain regions. Indeed,
399 in the hippocampus, it is likely that the local microenvironment plays a significant role in the
400 genesis of microglial aging, as regional distinctions in cellular function and composition – even in
401 apposed subregions – elicit different outcomes in microglia with age and following exposure to an
402 aged systemic environment. With age, multiple hippocampal subregions accumulate activated
403 microglia beginning at 12 months of age, signifying that age-related alterations in microglia are
404 initially present at middle age. Studying microglia, or other cell types, at these early stages of
405 aging in a region-specific manner could represent useful models to investigate the ontogeny of
406 aging without the confounding effects of accumulated functional deficits. Alternatively, the lack of
407 age-related accumulation of activated microglia in the molecular layer and inner CA1,
408 hippocampal subregions rich in synaptic terminals, points towards microenvironmental influences
409 that may prove refractory to aging.

410 Of note, we find that an inflammatory trajectory of microglia aging can be mitigated *in vitro*
411 by environmental TGFβ signaling, while loss of microglia-derived TGFB1 promoted progression
412 along aging-associated inflammatory trajectories *in vivo*. Together, these data indicate that TGFβ
413 signaling is necessary for maintaining youth-associated homeostasis and represents a modulator
414 in mediating advancement along aging-associated inflammatory trajectories. Furthermore, our
415 results, combined with those of Bedolla *et al*[34], strongly suggest that TGFβ signals in an autocrine
416 fashion to return microglia to a homeostatic state after encountering stressful stimuli. Functionally,
417 loss of microglia-derived TGFB1 resulted in hippocampal-dependent cognitive impairments in an
418 age-dependent manner, suggesting that advancement through aging-associated trajectories may
419 facilitate age-related cognitive decline. Given that a transient increase in *Tgfb1* expression is
420 observed in middle-aged microglia, it is possible that maintaining stress response-mediated
421 signaling into older ages may also provide a means to delay age-related microglial dysfunction
422 and maintain cognitive function. Alternatively, TGFβ signaling impairs microglial responses to

423 Alzheimer's disease pathology[51], suggesting that the dynamic regulation of TGFβ signaling in
424 response to aging-associated pathologies is necessary for tuning microglial responses.
425 While microglia have been demonstrated to mediate the establishment of cognitive
426 function during development[2] and play prominent roles in neurodegeneration[52], little is known
427 about how age-related changes in microglia affect cognitive function. The specificity of the
428 cognitive deficits that we observe in *Tgfb1* Het and *Tgfb1* cKO mice suggests that age-related
429 changes in microglia-derived TGFB1 predominantly impacts hippocampal-dependent cognitive
430 decline. Furthermore, the deficits observed in *Tgfb1* heterozygous mice point to the importance
431 of maintaining youthful levels of microglia-derived TGFB1 to counteract stressors that accrue
432 during aging.
433 Altogether, our results highlight the need to investigate aging across the lifespan in a
434 region-specific manner to reveal necessary cellular intermediates in the aging process. While the
435 present study focuses on age-related changes in microglia, our findings have broad implications
436 for other studies in determining the extent to which aging sequelae are conserved across different
437 cell types in the hippocampus. Furthermore, therapeutic interventions targeting intermediate
438 states in the aging process hold far reaching potential to counteract the development of age-
439 related pathologies, including those promoting cognitive dysfunction.
440
441
442
443
444
445
446
447
448
449
450
451
452
453
454
455
456

ACKNOWLEDGMENTS

We thank Dr. Erik Ullian for critically reading manuscript. **Funding**: This work was funded by National Institute on Aging (AG055292 (J.M.S.), AG055797 (S.A.V.), AG077816 (S.A.V.)), Simons Foundation (S.A.V). The authors declare no competing financial interests.

AUTHOR CONTRIBUTIONS

J.M.S and S.A.V. developed concept and designed experiments. J.M.S conducted experiments, collected data, and performed analysis. J.M.S and S.A.V wrote manuscript. S.A.V supervised all aspects of the project. All authors had the opportunity to discuss results and comment on manuscript.

COMPETING INTEREST STATEMENT

The authors declare no competing interests.

Fig. 1 | Hippocampal microglia exhibit progressive age-related transcriptional inflammatory activation. A, UMAP plot of microglia separated into transcriptional clusters. (n = 1 pool of 5 animals for each age) **B,** Superimposition of ages onto the UMAP plot with dashed lines signifying relative cluster demarcation. **C,** Percent composition of each cluster by age. **D,** Dot plot of expression of cluster markers sorted by age. Percent of cells expressing the gene and average normalized expression are represented. **E,** Violin plots of genes with dynamic age-related expression patterns. **F,** Representative images and quantification of C1q (yellow), C3 (red), and Iba1 (cyan) staining in the hilus and molecular layer (ML) of 6- and 24-month-old mice. (n=4-5 mice per group; mixed effects analysis followed by Dunnett's multiple comparisons; *P<0.05, **P<0.01, ****P<0.0001). **G,** Number of differentially expressed genes from the 6-month timepoint at each age. Bars above the intersect represent increased expression and those below represent decreased expression. **H,** The average expression change at all ages for genes differentially regulated genes at individual ages represented by the color scheme in **B**. **I, J, K,** Volcano plots of differentially expressed genes in microglia between 6- and 12-months (**I**), 6- and 18-months (**J**), and 6- and 24-months (**K**) and corresponding gene ontology analysis of genes with significantly increased (brown) or decreased (green) expression for each comparison. Data are shown as mean±s.e.m.

Fig. 2 | Hippocampal microglia aging advances through intermediate states that respond to systemic interventions or disease states. A, Pseudotime trajectories of microglia from an anchor point located in 6-month microglia presented in a UMAP plot. (n = 1 pool of 5 animals for each age) **B,** Microglia ages superimposed over pseudotime trajectories. **C,** Gene expression modules representing sections of the inflammatory aging trajectory over the right half of the UMAP plot (left). Modules were discovered using Moran's I autocorrelation test. Top Gene Ontology terms and representative genes in each module (right). **D,** Dotplot of pseudotime modules sorted by age. Percent of cells expressing the gene and average normalized expression are represented. **E, F, G,** Average gene expression changes for each aging module represented as log2 fold change of 12-months (**E**), 18-months (**F**), or 24-months (**G**) over 6-months. **H,** Representative images and quantification of KLF2 (magenta) and IBA1 (cyan) staining in the hippocampus across ages. (n=3 mice per group; one-way ANOVA with Tukey's post-hoc test; *P<0.05)**. I,** Diagram of the heterochronic parabiosis model with the comparisons made in scRNA-Seq. **J,** Representative images and quantification of CD68 (red) and IBA1 (cyan) staining in the hippocampus of isochronic young (IY) and heterochronic young (HY). (n=5 mice per group; unpaired Student's T-test; ***P<0.001)**. K,** Average gene expression changes for each aging module represented as log2 fold change of heterochronic young (HY) over isochronic young (IY) adult parabionts. Data from Palovics *et al* [38]. **L,** Diagram of microglia surrounding an Aβ plaque. **M,** Average gene expression changes for each aging module represented as log2 fold change of the $App^{NL\text{-}G\text{-}F}$ genotype (AD) over wildtype (WT). Data from Sala Frigerio *et al* [17]. (one sample T-test with the expected value of 0 (no change); *P<0.05, **P<0.01, ***P<0.001, ****P<0.0001). Data are shown as mean±s.e.m.

Fig. 3 | Intermediate states of microglia aging act as checkpoints on inflammatory progression. A, Representation of the microglia aging trajectory over the UMAP plot highlighting the region of peak *Tgfb1* expression. **B,** Representative RNAscope images and quantification of *Tgfb1* (red) expression in IBA1 (cyan) cells across ages. (n=5 per group; one-way ANOVA with Dunnett's post-hoc test; *P<0.05)**. C,** Dotplot of the expression values of TGFB1 signaling components from scRNA-Seq of aging hippocampal microglia (6-, 12-, 18-, and 24-month-old). Percent of cells expressing the gene and average normalized expression are represented. **D,** Schematic of the heterochronic parabiosis model and quantification of hippocampal microglia expression of *Tgfb1* from isochronic young (IY) and heterochronic young (HY) adult parabionts. Data derived from Pálovics *et al*[37]. **E,** Top gene ontology terms for the set of genes with significantly decreased expression in bulk microglia RNA-Seq following TGFB1 treatment compared to control (DMSO) in LPS treated microglia. (n=5 per group) **F,** Heatmap of top 10 genes in each aging module following TGFB1 compared to DMSO in LPS treated microglia. **G,** Average gene expression changes for each aging module represented as log2 fold change of TGFB1 treatment over DMSO. (one sample T-test with the expected value of 0 (no change); *P<0.05, ***P<0.001, ****P<0.0001). **H,** Representation of the microglia aging trajectory over the UMAP plot highlighting the stage where CX-5461 modulates the trajectory. **I,** Representative images of S6 (magenta) and Iba1 (cyan) staining in the hippocampus of 6- and 24-month-old mice and quantification across aging. (n=3 mice per group; one-way ANOVA with Tukey's post hoc test; *P<0.05, **P<0.005, ****P<0.0001). **J,** Schematic of the heterochronic parabiosis model and quantification of hippocampal microglia expression of translation module from isochronic young (IY) and heterochronic young (HY) adult parabionts. Data derived from Pálovics *et al*[37]. (one sample T-test with the expected value of 0 (no change); **P<0.01). **K,** Top gene ontology terms for the set of genes with significantly decreased expression in bulk microglia RNA-Seq following CX-5461 treatment compared to control (DMSO) in LPS treated microglia. (n=3 per group) **L,** Heatmap of top 10 genes in each aging module following CX-5461 compared to DMSO in LPS treated microglia. **M,** Average gene expression changes for each aging module represented as log2 fold change of CX-5461 treatment over DMSO. (one sample T-test with the expected value of 0 (no change); *P<0.05, **P<0.01, ****P<0.0001).

Fig. 4 | Targeting age-related changes in microglia-derived TGFB1 promotes microglia advancement along inflammatory trajectories in the hippocampus and impairs cognition. **A,** Schematic of *in vivo* manipulation schema of Module 2. Mature (7-8 months) littermate *Cx3cr1-Cre-ER*$^{+/wt}$; *Tgfb1*$^{flox/flox}$ (cKO), *Cx3cr1-Cre-ER*$^{+/wt}$; *Tgfb1*$^{flow/wt}$ (Het), and *Cx3cr1-Cre-ER*$^{+/wt}$; *Tgfb1*$^{wt/wt}$ (WT) mice were administered tamoxifen and subject to hippocampal microglia scRNA-Seq and behavior analysis two months later. **B,** UMAP plot of microglia separated into transcriptional clusters. (n = 2 pools of 3 animals per genotype) **C,** Stacked bar plot of the normalized relative percentage of cells of each genotype in the identified clusters. **D,** Dot plot of expression of aging module markers sorted by genotype. Percent of cells expressing the gene and average normalized expression are represented. **E,F,** Average gene expression changes for each aging module represented as log2 fold change of either Het over WT (**E**) or KO over WT (**F**). (one sample T-test with the expected value of 0 (no change); *P<0.05, ****P<0.0001)**. G,** Novel object recognition task. (Top) Diagram of the training and testing phases of the novel object recognition paradigm. (Bottom) Quantification of the NOR testing phase represented as percentage of time spent with the novel object (over the total time spent interacting with the objects). (n=9-13 per genotype; one sample T-test with the expected value of 50 (equal time spent with each object); ***P<0.001)(differences between groups determined by one-way ANOVA; **P<0.01)**. H,** Contextual fear conditioning. (Top) Diagram of the fear conditioning paradigm. (Bottom) Quantification of the percentage of time mice froze in the contextual fear conditioning testing phase. (n=14-16 per genotype; one-way ANOVA; *P<0.05). Data are shown as mean±s.e.m. **I,** Schematic of *in vivo* manipulation of *Tgfb1* at young and mature ages. Young (2 month) or mature (7-8 months) littermate *Tmem119-Cre-ER*$^{+/wt}$; *Tgfb1*$^{flox/flox}$ (cKO), *Tmem119-Cre-ER*$^{+/wt}$; *Tgfb1*$^{flow/wt}$ (Het), and *Tmem119-Cre-ER*$^{+/wt}$; *Tgfb1*$^{wt/wt}$ (WT) mice were administered tamoxifen and subject to behavioral analysis two months later. **J,K,** Quantification of the NOR testing phase represented as percentage of time spent with the novel object (over the total time spent interacting with the objects) for young (**J**) and mature (**K**) *Tmem119-Cre-ER*::*Tgfb1* mice. (n=12-26 in young and n=10-16 in mature mice per genotype; one sample T-test with the expected value of 50 (equal time spent with each object); *P<0.05, ***P<0.001).

695 **METHODS**

696 **Mice**

697 All animal procedures were performed in accordance with protocols approved by the UCSF
698 IACUC. Animals were housed in SPF barrier facilities and provided continuous food and water
699 along with environmental enrichment. Aging characterizations were performed on an inhouse
700 C57BL/6J mouse colony where 2-month-old mice were purchased from Jackson Laboratories
701 (Stock 000664) and aged in the UCSF Parnassus barrier facility. Timed pregnant females were
702 obtained for isolation of primary microglia from newborn pups. Male mice were used in all
703 experiments. B6.129P2(Cg)-*Cx3cr1*$^{tm2.1(cre/ERT2)Litt}$/WganJ (*Cx3cr1*Cre^{ER}) (Stock 021160) and
704 C57BL/6J-Tgfb1^{em2Lutzy}/Mmjax (*Tgfb1*-flox) (Stock 65809-JAX) mice were obtained from Jackson
705 Laboratories. Mice were bred to obtain *Cx3cr1*Cre^{ER} +/wt with either *Tgfb1* wt/wt, *Tgfb1* fl/fl. As
706 *Cx3cr1*Cre^{ER} is a knock-in/knock-out allele for the microglia homeostatic gene *Cx3cr1*, all mice
707 tested were *Cx3cr1*Cre^{ER} +/wt. To induce recombination and deletion of *Tgfb1* by Cre^{ER}, we
708 injected tamoxifen for 5 days at 90mg/kg daily, and mice were analyzed after 60 days.

709

710 **Parabiosis**

711 Parabiosis surgery followed previously described procedures[53]. Mirror-image skin incisions at the
712 left and right flanks were made through the skin, and shorter incisions were made through the
713 peritoneum. The peritoneal openings of the adjacent parabionts were sutured together with
714 chromic gut suture (MYCO Medical, GC635-BRC). Apposing elbow and knee joints from each
715 parabiont were sutured together (Coated VICRYL Suture, Ethicon, J386) and the skin of each
716 mouse was stapled (9-mm Autoclip, Clay Adams, 427631) to the skin of the adjacent parabiont.
717 Each mouse was injected subcutaneously with Carpofen, Enrofloxacin, and Buprenex as directed
718 for pain and monitored during recovery. For overall health and maintenance behavior, several
719 recovery characteristics were analyzed at various times after surgery, including pair weights and
720 grooming behavior.

721

722 **Bulk Microglia RNA-Seq**

723 Microglia were isolated from C57BL6/J, *Tgfb1* cHet, and *Tgfb1* cKO using FACS. Briefly, mice
724 were sedated with ketamine followed by perfusion with 30mL of ice-cold PBS. The entire brain
725 was removed, then the hippocampus was sub-dissected. Single-cell suspensions were generated
726 by enzyme-mediated (papain) and mechanical dissociation using Miltenyi Neural Dissociation Kits
727 (P) (Miltenyi, 130-092-628) according to the manufacturer's instructions. Myelin was depleted
728 from the suspensions using Myelin Removal Beads (Miltenyi, 130-096-731). Cells were labeled

729 with CD11b-APC (eBioscience, 17-0112-82, RRID:AB_469343) and CD45-PE (eBioscience, 12-
730 0451-82, RRID:AB_465668), then sorted at 4°C into Tri Reagent with a FACS AriaII (BD). The
731 gating strategy for microglia isolation is presented in Figure S1D, showing the collection of
732 $Cd11b^{+}Cd45^{Intermediate}$ cells. During the collection of control and *Tgfb1* microglia, CD48 was
733 detected in $Cd11b^{+}Cd45^{Intermediate}$ cells using CD48-Pacific Blue (BioLegend, 103417,
734 RRID:AB_756139). FlowJo was used to analyze flow cytometry data. RNA was isolated from
735 microglia using Tri Reagent (Sigma-Aldrich, T9424). RNA pellets were resuspended in 5uL TE
736 buffer.
737
738 RNA was transformed into RNA-Seq libraries using an adapted version of the Smart-Seq2
739 protocol[54]. Briefly, 5ng of total RNA was reverse transcribed with SuperScript II (Thermo Fisher,
740 18064014) supplemented with betaine and $MgCl_2$ using an oligo-dT RT primer
741 (AAGCAGTGGTATCAACGCAGAGTACT(30)VN) with a PCR binding site and a template
742 switching oligonucleotide (5′ AAGCAGTGGTATCAACGCAGAGTACATrGrG+G) with a
743 homotypic PCR binding site. Betaine and MgCl2 were added to enhance the reaction. After
744 reverse transcription, whole transcriptome amplification by PCR was performed for 12 cycles
745 using KAPA HiFi HotStart ReadyMix (Roche, 7958935001) with a PCR primer
746 (AAGCAGTGGTATCAACGCAGAGT). The PCR reaction was cleaned up with Ampure XP beads
747 (Beckman Coulter, A63881). In addition, after the whole transcriptome PCR amplification step,
748 qPCR was performed to determine the presence of microglia-specific transcripts (*Cx3cr1*) and
749 housekeeping genes (*Gapdh*). The amplified DNA was diluted to a concentration of 0.5ng/ul, and
750 subjected to tagmentation with the Illumina Nextera XT kit (Illumina, FC-131-1096). Each sample
751 was PCR amplified with a unique set of Nextera indices. Bulk microglia RNA-Seq libraries were
752 sequenced on an Illumina HiSeq, while *in vitro* microglia RNA-Seq libraries were sequenced on
753 an Illumina Nova-Seq.
754
755 **RNA-Seq Analysis**
756 FASTQ reads were pseudo aligned to the mouse transcriptome (GRCm39 cDNA from Ensembl)
757 using kallisto[55] with default parameters. Next, transcript abundance estimates were imported into
758 DeSeq2[56]. Differential expression analysis was performed using DeSeq2 using the Wald
759 significance test. Gene ontology analysis was performed with Panther[57-59]. Principal component
760 analysis plots were generated with the plotPCA function included with DeSeq2 and graphed with
761 ggplot2. Heatmaps were generated with the pheatmap package in R.

762 The overlap between gene expression differences in aging and LPS treatment were
763 determined using genes significantly changed between the 6- and 24-month-old timepoints in the
764 scRNA-Seq data and the control and LPS treated primary microglia. χ^2 test was used to determine
765 the significance of the overlap between these two datasets. The Venn diagram was generated
766 using the VennDiagram package in R.
767
768 **10x Genomics Single Cell RNA-Sequencing**
769 10x Single-Cell RNA-Seq libraries were generated from Cd11b+ cells isolated from the
770 hippocampi of an aging cohort of mice consisting of 6-, 12-, 18-, and 24-month-old C57BL/6J mice
771 that were all collected and processed on the same day in an interspersed order. Mice were
772 sedated with ketamine followed by perfusion with ice-cold PBS. Subsequently, the entire brain
773 was removed from the mouse followed by sub-dissection of the hippocampus. For each age,
774 hippocampi from five mice were pooled during the dissection step in HBSS at 4°C. Single-cell
775 suspensions were generated by enzyme-mediated (papain) and mechanical dissociation using
776 Miltenyi Neural Dissociation Kits (P). The papain dissociation was done at 37°C for 10 minutes
777 with 3 trituration steps. All other processing steps were performed at 4°C. Myelin was depleted
778 from the suspensions using Myelin Removal Beads (Miltenyi). Microglia were enriched using
779 Cd11b magnetic beads (Miltenyi, 130-126-725). Cell viability was determined to be over 95%.
780 Single-cell RNA-Seq 3' libraries were generated from the cell suspension using 10x Genomics
781 Chromium Single-Cell 3' Solution. Libraries were sequenced on the Illumina Nova-Seq. Cell
782 Ranger demultiplexed and mapped (using bcl2fastq) reads, followed by alignment (with STAR),
783 and generation of single-cell expression matrices[60].
784 The isolation protocol for the *Tgfb1* genetic mouse model was modified. We added
785 transcriptional and translational inhibitors (Actinomycin D (Sigma-Aldrich, A1410), Anisomycin
786 (Sigma-Aldrich, A9789), and Triptolide (Sigma-Aldrich, T3652) to prevent transcriptional changes
787 due to *ex vivo* activation [61]. We utilized the concentrations presented in Marsh *et al*. 2022[61].
788
789 **Single-cell RNA-Seq Analysis**
790 Seurat: The single-cell gene expression matrices generated by Cell Ranger were loaded into
791 Seurat[62].
792
793 Aging microglia dataset. Cells were filtered according to the following parameters: Genes > 1000
794 & RNA count > 10000 & mitochondrial percentage < 5. The count data was log normalized. The
795 2,500 most variable genes were identified using the "vst" method. The expression data was scaled

796 and centered. Principal component analysis was performed, and the first 25 PCAs were used to
797 identify nearest neighbors, and interconnected clusters were identified with a resolution of 0.4.
798 UMAP was used to visualize the results. Preliminary dimensionality reduction and visualization
799 with UMAP using 25 PCAs and 25 nearest neighbors in Seurat identified a large microglia cluster,
800 plus sparse clusters consisting of astrocytes, vascular cells, neutrophils, and macrophages. *Hexb*,
801 *P2ry12*, *Tmem119*, and *Slc2a5* are used as markers to identify microglia in the preliminary
802 clustering, while *Nrxn1* (neurons), *Tm4sf1* (vasculature), *Dclk*1 (astrocytes), *Sdpr* (vasculature
803 smooth muscle), *Abcb1a* (pericyte/vasculature), and *Foxq1* (macrophages) identified other cell
804 types. The data was then subsetted on the non-proliferating microglial clusters (to avoid
805 confounds associated with the cell cycle). The top 1,500 most variable genes in the subsetted
806 microglia were identified using the "vst" method. The data was scaled and centered. Principal
807 component analysis was performed, and the first 8 PCAs were used to identify nearest neighbors,
808 and interconnected clusters were identified with a resolution of 0.25. UMAP was used to visualize
809 the results using 8 PCAs and 100 nearest neighbors. Gene enrichment and differential expression
810 analysis was performed on the filtered dataset to determine differences between ages.
811
812 *Tgfb1* cKO microglia dataset. Cells were prefiltered according to the following parameters: Hexb
813 > 4 & Tmem119 > 1 & Cx3cr1 > 4 & Top2a < 1 & Mki67 < 1 nFeature_RNA > 1000 &
814 nFeature_RNA < 6000 & nCount_RNA > 2000 & nCount_RNA < 40000 & percent.mt <10. Data
815 was integrated using IntegrateData and scaled. Principal component analysis was performed,
816 and the first 50 PCAs were used to identify nearest neighbors, and interconnected clusters were
817 identified with a resolution of 0.35. UMAP was used to visualize the results. Preliminary
818 dimensionality reduction and visualization with UMAP using 50 PCAs identified a large microglia
819 cluster, plus clusters of other cell types. The non-proliferative microglia clusters were subsetted
820 for further analysis (the macrophage cluster was differentiated from the microglia cluster based
821 on increased expression of *Mcp1, Pf4,* and *Ms4a7*). The data was scaled and centered. Principal
822 component analysis was performed, and the first 10 PCAs were used for UMAP dimensionality
823 reduction and to identify nearest neighbors, and interconnected clusters were identified with a
824 resolution of 0.20.
825
826 Monocle 3: Monocle 3 was used to generate the pseudotime analysis[63-66]. Data was imported
827 from Seurat analysis and a Monocle dataset was generated. The dataset was preprocessed with
828 normalization of the data and PCA generation. Next, the preprocessed data underwent further
829 non-linear dimensionality reduction using UMAP. Cells were clustered, and trajectories were

830 determined for cells within a cluster. For determining “pseudotime” aging of microglia, the root
831 node of the pseudotime trajectory was manually placed in the cluster of 6-month cells. The graph
832 segments of the pseudotime trajectories resulting in inflammatory activation were chosen for
833 further analysis. Graph autocorrelation analysis was performed on the inflammatory trajectory
834 using Moran’s I, which determines if genes are expressed in focal regions of graph space. A cutoff
835 q-value of 0.005 was set as significant for focal expression. Subsequently, coregulated modules
836 were determined using Louvain community analysis at an optimized resolution of 0.0078. The
837 modules were then overlaid onto the UMAP plot to determine the region of the trajectory with focal
838 expression of the module. The ten most significant genes of each module, as determined by q-
839 value were used to construct the heatmaps in Figures 3F and 3I. The significant genes of each
840 module were used to determine the effects of manipulations in the presence of LPS in Figure 3J.
841
842 Scorpius: Scorpius was used to generate a secondary pseudotime analysis that confirmed the
843 results of the Monocle 3 analysis[67]. Data was imported from Seurat analysis as a
844 SingleCellExperiment and dimensionality was reduced. A trajectory plot was generated followed
845 by a trajectory inference. Candidate marker genes were identified using the gene_importances
846 command. Subsequently, gene expression modules were generated with the extract_modules
847 command and visualized using a heatmap.
848
849 **Immunohistochemistry**
850 Mice were sedated with ketamine followed by perfusion with 30mL of ice-cold PBS. Brains were
851 collected from PBS perfused mice and fixed overnight at 4°C in 4% paraformaldehyde in PBS.
852 The brains were washed with PBS and immersed in 30% sucrose (in PBS), and then stored at
853 4°C until the brains sank. 40μM coronal sections were sliced using a microtome at -20°C. Sections
854 were stored in cryopreservation buffer (40% PB Buffer (0.02 M Sodium Phosphate Monobasic,
855 0.08 M Sodium Phosphate Dibasic, pH 7.4), 30% Glycerol, 30% Ethylene Glycol) at -20°C until
856 staining. Hippocampal sections were washed three times in TBST. Sections were permeabilized
857 in pretreatment buffer (0.1% Triton-X in TBST) with rocking for 1 hour at room temperature. After
858 three washes in TBST, sections were blocked in 5% goat serum for 2 hours (for IBA1/CD68
859 double stain) or 5% donkey serum (NFKB/Iba1 and C1q/C3/Iba1 stains). Blocking buffer was
860 replaced with primary antibody mixture and incubated overnight at 4°C with rocking. The following
861 primary antibodies were used: rabbit anti-IBA1 (1:1000, Wako, Cat# 019-19741,
862 RRID:AB_839504), rat anti-CD68 (1:250, Bio-Rad, Cat# MCA1957, RRID:AB_322219), rabbit
863 anti-NFKB p65 (1:500, Santa Cruz, Cat# sc-372, RRID:AB_632037), guinea pig anti-Iba1 (1:1000,

Synaptic Systems, Cat# 234-004, RRID:AB_2493179), rabbit anti-C1q (1:1000, Abcam, Cat# ab182451, RRID:AB_2732849), rat anti-C3 (1:1000, Abcam, Cat# ab11862, RRID:AB_2066623), rabbit anti-S6 (1:500, Cell Signaling, Cat# 2217, RRID:AB_331355), and rabbit anti-KLF2 (1:250, Bioss, Cat# bs-2772R, RRID:AB_10857057). The sections were washed three times with TBST. Subsequently, secondary antibody solution was added to the sections, and incubated at room temperature with rocking for two hours. The following secondary antibodies were used: goat anti-rabbit AlexaFluor 488 (Life Technologies, Cat# A-11008, RRID:AB_143165), goat anti-rat AlexaFluor 555 (Life Technologies, Cat# A-21434, RRID:AB_2535855), donkey anti-guinea pig AlexaFluor 488 (Jackson Immuno, Cat# 706-545-148, RRID:AB_2340472), donkey anti-rabbit AlexaFluor 555 (Life Technologies, Cat# A-31572, RRID:AB_162543), and donkey anti-rat AlexaFluor 647 (Jackson Immuno, Cat# 712-606-150, RRID:AB_2340695). The sections were washed three times with TBST, with the first wash containing Hoescht 33342 (Invitrogen, H3570) at a concentration of 1μg/mL. The sections were transferred to phosphate buffer and mounted on frosted slides. Coverslips were mounted with Prolong Gold Antifade (Thermo Fisher, P10144) reagent after the sections were dried. Slides were imaged at 20x magnification on a Zeiss LSM 800 or LSM900 for a final resolution of 0.312μM/pixel. 8-9 z-planes were imaged at 3μM intervals. The hippocampus was imaged, and the tiled images were stitched together with Zeiss ZenPro software. 2-3 hippocampal sections were imaged from each sample.

Images were analyzed with FIJI. Maximum intensity projections of Z-stacked images were constructed. Images were converted to 8-bit images and consistent adjustments were made for each channel within an experiment. The Iba1 channel was used to quantify microglia using the particle counter function in FIJI and the counts were validated by manual visual counting. The presence of CD68, NFKB(p65), C3, or C1q in microglia was determined by creating ROIs within the microglia in a field using the create selection function on the Iba1 images. The ROIs of the hippocampal subregions and the microglia were combined, and CD68 puncta meeting a minimum particle size threshold (100 pixels, equating to 31.2μM) within microglia determined if the microglia were activated (CD68+IBA1+), while the measure function determined the intensity of NFKB(p65), C3, or C1q. To determine percent activation of microglia with IBA1/CD68 staining, we divided the number of microglia that were activated (CD68+IBA1+) by the total number of microglia (IBA1+) in the analyzed regions and multiplied by 100.

Additionally, we tested whether autofluorescence from aged tissue was interfering with our signal using TrueBlack® Lipofuscin Autofluorescence Quencher (Cell Signaling, Cat #92401). Using the

898 IBA1/CD68 doublestain, we obtained very similary results for microglia activation. Furthermore,
899 our KLF2 stain was performed with TrueBlack.
900
901 ***In vitro* treatment of microglia**
902 Mixed glial cultures were generated from p1 male pups. Cortices and hippocampi were isolated
903 from the pups, and meninges were removed. The tissue was broken up by repeatedly pipetting
904 up and down, followed by dissociation with Trypsin. Single cell suspensions were plated on poly-
905 L-lysine coated flasks in DMEM (Thermo Fisher, 11965-118) supplemented with 10% FBS
906 (Gemini Bio-Products, 900-208) and antibiotic mix (Penicillin/Streptomycin)(Genesee Scientific,
907 25-512) and incubated at 37°C in 5% CO_2. Media was changed after 4 days to remove debris.
908 Microglia were isolated after 14 days by agitating the plates to dislodge microglia, then transferring
909 the supernatant of each sample evenly amongst 4 wells of a 24 well plate. Microglia were
910 incubated for 16 hours followed by replacement with serum free macrophage SFM media (Thermo
911 Fisher, 12065074) supplemented with M-CSF (10ng/m) (Peprotech, 315-02) and antibiotic mix.
912 After 24 hours microglia were treated with RNA polymerase I Inhibitor 2, CX-5461 (100nM)(EMD
913 Millipore, 509265) or human TGFβ1 recombinant protein (10ng/mL)(ThermoFisher Scientific,
914 PHG9204) for 24 hours followed by addition of lipopolysaccharides (LPS, 200ng/uL) from *E. coli*
915 (Sigma-Aldrich, L2018) for 8 hours and ATP (10nM)(InvivoGen, tlrl-atpl) for 30 minutes. Tri
916 Reagent was added to the culture plate, and the plates were shaken for 5 minutes. RNA was
917 isolated according to manufacturer's instructions. RNA-Seq libraries were generated as above for
918 the bulk RNA-Seq.
919
920 **RNAscope**
921 RNAscope was performed with the RNAscope® Multiplex Fluorescent Reagent Kit v2 (ACD,
922 323110). 40μM coronal sections were washed with TBST, then incubated with hydrogen peroxide
923 for 45 minutes at 25°C. After washing with TBST, the sections were incubated in Target Retrieval
924 Buffer at 95°C for 10 minutes. The sections were mounted on slides and dried overnight. The
925 sections were treated with RNAscope Protease III for 10 minutes at 40°C. Sections were washed
926 in water four times. Sections were incubated with *Tgfb1* probe (ACD, 443571-C2) for 2 hours at
927 40°C. The sections were washed twice with RNAscope wash buffer. The sections were incubated
928 with AMP1 for 30 minutes, AMP2 for 30 minutes, AMP3 for 15 minutes, HRP-C2 for 15 minutes,
929 TSA Plus Cy3 (1:1000, Perkin Elmer, SKU NEL744001KT) for 30 minutes, and HRP-Blocker for
930 15 minutes; all at 40°C with washes with RNAscope wash buffer between every incubation. RNA-

931 Protein Co-Detection Ancillary Kit (ACD, 323180) buffer was used to block the sections before
932 incubating with rabbit anti-IBA1 (1:500, Wako, Cat# 019-19741, RRID:AB_839504) overnight at
933 4°C. Sections were washed three times in TBST. Sections were incubated with secondary
934 antibody solution with goat anti-rabbit AlexaFluor 488 (1:1000, Life Technologies, Cat# A-11008,
935 RRID:AB_143165) for two hours at room temperature. The sections were washed three times
936 with TBST, with the first wash containing Hoescht 33342 (Invitrogen, H3570) at a concentration
937 of 1μg/mL Coverslips were mounted with Prolong Gold Antifade (Thermo Fisher, P10144) reagent
938 after the sections were dried. Slides were imaged at 40x magnification on a Zeiss LSM 900. 10
939 z-planes were imaged at 1μM intervals.
940
941 Images were analyzed with FIJI. Maximum intensity projections of Z-stacked images were
942 constructed. Images were converted to 8-bit images and the *Tgfb1* was thresholded. For each
943 section, the intensity of 5-7 individual *Tgfb1* puncta were averaged to get the average puncta
944 intensity of that section. The intensity of all *Tgfb1* signal in clearly identifiable individual IBA1 cells
945 was measured for 20-25 cells in the molecular layer of the hippocampus. The mean *Tgfb1* count
946 per microglia for each sample was calculated by dividing the average *Tgfb1* intensity in IBA1 cells
947 by the average puncta intensity.
948
949 **Contextual fear conditioning**
950 In this task, mice learned to associate the environmental context (fear conditioning chamber) with
951 an aversive stimulus (mild foot shock; unconditioned stimulus, US) during the training phase
952 enabling testing for hippocampal- dependent contextual fear conditioning. To also assess
953 amygdala-dependent cued fear conditioning, the mild foot shock was paired with a light and tone
954 cue (conditioned stimulus, CS) during the training phase. Conditioned fear was displayed as
955 freezing behavior. Specific training parameters are as follows: tone duration is 30 seconds; level
956 is 70 dB, 2 kHz; shock duration is 2 seconds; intensity is 0.6 mA. This intensity is not painful and
957 can easily be tolerated but will generate an unpleasant feeling. More specifically, on day 1 each
958 mouse was placed in a fear-conditioning chamber and allowed to explore for 2 min before delivery
959 of a 30-second tone (70 dB) and light ending with a 2-second foot shock (0.6 mA). Two minutes
960 later, a second CS-US pair was delivered. On day 2, each mouse was first placed in the fear-
961 conditioning chamber containing the same exact context, but with no CS or foot shock. Freezing
962 was analyzed for 2 minutes and represented as the percentage of time that the mouse froze over
963 the 2 minutes. One hour later, the mice were placed in a new context containing a different odor,
964 floor texture, chamber walls and shape. Animals were allowed to explore for 2 minutes before

being re-exposed to the CS. Freezing was analyzed for 30 seconds following the CS and represented as the percentage of time that the mouse froze over those 30 seconds. Determination of freezing behavior was performed using FreezeScan video tracking system and software (Cleversys, Inc). Single outliers were removed using the extreme studentized deviate method (Grubbs' test) with an alpha of 0.05.

Novel object recognition

The novel object recognition task was adapted from a previously described protocol[68]. Specifically, during the habituation phase (day 1), mice could freely explore an empty open field arena for 10 minutes (motor activity and anxiety (time in center) were measured during this phase). During the training phase (day 2), two identical objects were placed in the habituated arena, and mice could explore the objects for 5 minutes. For the testing phase (day 3), one object was replaced with a novel object, and mice could explore the objects for 5 minutes. Time spent exploring each object was quantified using the Smart Video Tracking Software (Panlab; Harvard Apparatus). Two different sets of objects are used. To control for any inherent object preference, half of the mice are exposed to object A as their novel object and half to object B. To control for any potential object-independent location preference, the location of the novel object relative to the trained object is also varied. The objects were chosen based on their ability to capture the animal's interest, independent of genetic background or age. To determine percent time with novel object, we calculate (Time with novel object)/(Time with Trained Object + Time with Novel Object) * 100. In this preference index, 100% indicates full preference for the novel object, and 0% indicates full preference for the trained object. A mouse with a value of 50% would have spent equal time exploring both objects. Mice that did not explore both objects for 5 seconds during the training phase or testing phase were excluded from analysis. Single outliers were removed using the extreme studentized deviate method (Grubbs' test) with an alpha of 0.05.

Y maze

The Y Maze task was conducted using an established forced alternation protocol[69]. During the training phase, mice were placed in the start arm facing the wall and allowed to explore the start and trained arm for 5 minutes, while entry to the 3rd arm (novel arm) was blocked. The maze was cleaned between each mouse to remove odor cues, and the trained arm was alternated between mice. The mouse was then removed to its home cage. After 30 minutes, the block was removed, and the mouse was returned to the start arm and allowed to explore all 3 arms for 5 minutes. Time spent in each arm was quantified using the Smart Video Tracking Software (Panlab; Harvard

Apparatus). The percent time in the novel arm was defined as time in the novel arm divided by time spent in the novel and trained arms during the task.

Datasets

All RNA-Seq and scRNA-Seq data have been deposited in the Gene Expression Omnibus and are publicly available as of the date of publication. The following datasets were generated for this manuscript and deposited in Gene Expression Omnibus: aging single-cell RNA-Seq (GSE179358), *in vitro* treated primary microglia (GSE179611), and *Tgfb1* cKO microglia RNA-Seq (GSE190007).

Statistics

Researchers were blinded throughout histological assessments with groups being un-blinded at the end of each experiment upon statistical analysis. Data are expressed as mean ± s.e.m with individual sample values being shown. Statistical analysis was performed with Prism 8.0 (GraphPad), R, DESeq2, Seurat, or Monocle 3. Comparisons of means in histology experiments were analyzed with multiple T-tests followed by Holm-Sidak correction or mixed effects analysis followed by Dunnett's multiple comparisons (Prism). Changes in expression for aggregated gene sets were determined with one sample T-tests with the expected value of 0 in log2 space (null hypothesis of no change). Differential expression analysis in DESeq2 was based on Wald's significance test of the negative binomial distribution. Differential expression analysis of single-cell RNA-Seq data in Seurat was performed using non-parametric Wilcoxon rank sum tests. Autocorrelation analysis to determine focal expression Monocle 3 was done using Moran's I. The significance of gene set overlap was determined using the χ^2 test with R. All data generated or analyzed in this study are included in this article.

1033 **SUPPLEMENTAL MATERIAL**

1034

1035 **Fig. S1 | Hippocampal microglia exhibit age-related heterogeneity during aging. A,** UMAP
1036 plot of all Cd11b+ cells. Several adjacent clusters of microglia were identified, as well as a cluster
1037 of proliferating microglia. Smaller populations of peripheral immune cell types – macrophages and
1038 neutrophils – were identified. Clusters of astrocytes and vascular cells were also found. Overall,
1039 greater than 82% of cells were microglia. (n = 1 pool of 5 animals for each age) **B,** Dot plot showing
1040 expression (average expression and percent of cells expressing) of top two markers for each
1041 cluster. **C,** UMAP plots with expression levels of microglia markers superimposed onto cells.
1042 Notice that peripheral immune cells express microglia markers; however, they are distinguished
1043 from microglia based on marker expression from (b). **D-G,** Volcano plots of differential gene
1044 expression for the clusters identified in Figure 1A compared to every other cluster for Homeostatic
1045 (**D**), Transition (**E**), Activation (**F**), and Interferon (**G**) microglia clusters. **H,** Cluster composition of
1046 non-proliferating microglia by age. **I,** Standardized variation of non-proliferating microglia for each
1047 age.

1048

1049

1050

1051

1052

1053

1054

1055

1056

1057

1058

1059

1060

1061

1062

1063

1064

1065

1066

Fig. S2 | Spatiotemporal kinetics of microglial inflammatory activation in the aging hippocampus. A, Diagram depicting ages utilized for immunohistochemical analysis. **B,** Diagram of the hippocampus labeled with the regions analyzed. **C,** Illustration of subregions analyzed by immunohistochemistry. **D,** Representative images and quantification of IBA1 (cyan)/CD68 (red)-positive microglia across hippocampal subregions in 3- and 24-month old mice. Scale bars are 10μM. (n=5 per group; T-test with Holm-Sidak correction; *P<0.05, **P<0.01) **E,** Heatmap of the quantification of activated microglia across ages and subregions. **F,** Representative wide field images of IBA1 (cyan)/CD68 (red) in the dentate gyrus in 3- and 24-month old mice. Scale bars are 100μM. **G,** Representative wide field images of Iba1 (cyan)/ NFKB p65 (yellow) in the dentate gyrus in 3- and 24-month old mice. Scale bars are 100μM. **H,** Representative images and quantification of Iba1 (cyan)/ NFKB p65 (yellow) staining across hippocampal subregions. Scale bars are 10μM. (n=5 per group; T-test with Holm-Sidak correction; *P<0.05, **P<0.01, ****P<0.0001) **I,** Heatmap of the quantification of NFKB signal in microglia across ages and subregions. n=4-5 mice per condition.

1101 **Figure S3 | Hippocampal microglia aging advances through intermediate states that**
1102 **respond to systemic interventions or disease states**. **A**, Volcano plot of differential gene
1103 expression of 12-month microglia versus all other ages with significant genes in teal. **B**, Gene
1104 ontology analysis of biological processes enriched in those genes with increased expression at
1105 12-months of age. **C**, Representative images and quantification of CD68 (red) and IBA1 (cyan)
1106 staining in the hippocampus of isochronic young (IY) and heterochronic young (HY) along with a
1107 diagram of the comparisons. (n=5 mice per group; unpaired Student's T-test; ***P<0.001)**.** Data
1108 are shown as mean±s.e.m. **D,** Dotplot of pseudotime modules in young (Y), isochronic young (IY),
1109 and heterochronic young (HY) parabiont microglia. Data is from Palovics *et al*[38]. Percent of cells
1110 expressing the gene and average normalized expression are represented. **E,** Volcano plots of
1111 differential gene expression of $App^{NL\text{-}G\text{-}F}$ genotype (AD) over wildtype (WT) microglia at 6- (left)
1112 and 12-months of age. Significant genes are in teal. Data is from Frigerio[70]. **F,** Dotplot of
1113 pseudotime modules across ages (3-, 6-, 12-, and 21-months old) and genotypes ($App^{NL\text{-}G\text{-}F}$
1114 genotype (AD) over C57Bl/6 (WT)). Data is from Frigerio[17]. Percent of cells expressing the gene
1115 and average normalized expression are represented.
1116
1117
1118
1119
1120
1121
1122
1123
1124
1125
1126
1127
1128
1129
1130
1131
1132
1133
1134

Fig. S4 | Intermediate states of microglia aging act as checkpoints on inflammatory progression. **A,** Quantification of percentage of *Tgfb1* RNAscope signal within IBA1 cells. **B**, Quantification of IHC of pTGFBR1 signal in IBA1 cells across ages. (n=4-5 mice per group; one-way ANOVA; *P<0.05) **C,** Quantification of the expression of TGFB1 signaling components from Figure 3C. Expression values for the genes are represented as Z-scores. (n=12 genes with reads in >25% of cells; Friedman test followed by Dunn's multiple comparisons test; *P<0.05, ***P<0.001) **D**, Dotplot of the expression values of TGFB1 signaling components in young (Y), aged (A), isochronic young (IY), and heterochronic young (HY) parabiont microglia. Data is from Palovics *et al*[38]. Percent of cells expressing the gene and average normalized expression are represented. UMAP plot of *Tgfb1* scRNA-Seq colored by genotype. **E**, Dotplot of the expression values of TGFB1 signaling components in aging microglia categorized by the expression of *Tgfb1* into quartiles with Q1 having the lowest expression of *Tgfb1* and Q4 having the highest expression. **F,** Quantification of the expression of TGFB1 signaling components from (**E**). Expression values for the genes are represented as Z-scores. (n=12 genes with reads in >25% of cells; Friedman test followed by Dunn's multiple comparisons test; *P<0.05, ***P<0.001) **G,** Dotplot of the expression values of selected TGFB signaling targets (activated and repressed, genes found in both Butovsky *et al.*[33] and Qin *et al*.[71]) in aging microglia categorized by the expression of *Tgfb1*. **H,** Heatmap of gene expression changes in the top 10 genes in each aging module induced by LPS. **I**, Overlap between microglia gene expression changes induced by LPS and aging. (χ^2<2.2e-16). **J**, PCA plot of pharmacological manipulations with or without LPS treatment.

Fig. S5 | Targeting age-related changes in microglia-derived TGFB1 promotes microglia advancement along inflammatory trajectories in the hippocampus.

A, Representative images and quantification of IBA1 (cyan)/CD68 (red)-positive microglia in wildtype, *Tgfb1* cHet, and *Tgfb1* cKO hippocampi. (n=3-5; one way ANOVA with Tukey post hoc test; *P<0.05) **B,** Dotplot of the expression values of TGFB1 signaling components from scRNA-Seq of *Tgfb1* WT, cHet, and cKO microglia. (n = 2 pools of 3 animals per genotype) **C,** UMAP plot of *Tgfb1* scRNA-Seq colored by genotype. **D,** FACS plots of gating strategy for microglia isolation for RNA-Seq in cHet and cKO hippocampi. Quantification of the flow cytometry analysis of CD11b and CD45. (n=3-5; mixed effects analysis; *P<0.05, ****P<0.0001). **E**, Example histogram and quantification of CD48 in control and *Tgfb1* cKO FACS-sorted microglia. (n=3-5 per group; T-test; ****P<0.0001). **F,** Top gene ontology terms associated with genes significantly increased in microglia bulk RNA-Seq in *Tgfb1* cKO samples (n=3-5 samples per genotype). **G**, Top gene ontology terms associated with genes significantly decreased in microglia bulk RNA-Seq in *Tgfb1* cKO samples. **H**, Overlap between concordant microglia gene expression changes induced by *Tgfb1* knockout and aging. (χ^2<2.2e-16). **I**, Heatmap of gene expression of the top 10 genes in each aging module in control and *Tgfb1* cKO microglia. **J**, Average gene expression changes for each aging module represented as log2 fold change of *Tgfb1* cKO over control. (one sample T-test with the expected value of 0 (no change); ****P<0.0001). Data are shown as means±s.e.m.

1203 **Fig. S6 | Targeting age-related changes in microglia-derived TGFB1 impairs cognition.**
1204 **A**, Freezing during the cued fear conditioning phase of the fear conditioning test for the *Cx3cr1-*
1205 *Cre-ER*::*Tgfb1* cohort. The percent freezing was calculated for the last 30 seconds of the test
1206 following the conditioned stimulus. (n=13-16 per genotype) **B**, Diagram and results of Y-maze test
1207 for the *Cx3cr1-Cre-ER*::*Tgfb1* cohort. Results are presented as preference for the novel arm
1208 versus the trained armed (time in novel arm/ (time in novel arm + trained arm) x 100). (n=14-16
1209 per genotype) **C**, Percent time in the center of the open field and distance traveled during the
1210 open field test for the *Cx3cr1-Cre-ER*::*Tgfb1* cohort. (n=14-16 per genotype) **D, F,** Results of Y-
1211 maze test for the young (**D**) and mature (**F**) *Tmem119-Cre-ER*::*Tgfb1* cohort. (n=8-16 per
1212 genotype for young and n=10-16 per genotype for mature) **E,G,** Percent time in the center of the
1213 open field and distance traveled during the open field test for the *Tmem119-Cre-ER*::*Tgfb1* cohort.
1214 (n=12-26 per genotype for young and n=10-16 per genotype for mature) Data are shown as
1215 mean±s.e.m.
1216
1217
1218
1219
1220
1221
1222
1223
1224
1225
1226
1227
1228
1229
1230
1231
1232
1233
1234
1235

Table S1 | Gene markers for each age group and differential expression between the 6- and 12-, 18-, or 24-month-old microglia in single-cell RNA-Seq of aging hippocampal microglia. The tables contain genes selectively increased or decreased in each age group when compared to every other age group combined and genes differentially expressed between 6- and 12-, 18-, or 24-month microglia. The tables contain the average log fold change, the percentage of cells in each group with expression, and the adjusted p-value.

Table S2 | Pseudotime trajectories of aging microglia. The pseudotime analysis contains the spatial autocorrelation analysis. Moran's I was used to detect focal expression of genes that were consequently constructed into co-regulated modules using Louvain community analysis. The table contains the adjusted p-value (q-value) and module information.

Table S3 | RNA-Seq analysis of primary microglia treated with LPS and TGFB1 or CX-5461. The tables contain the RNA-Seq differential expression analysis of control and LPS activated primary microglia, DMSO and CX-5461 treated primary microglia activated by LPS, and DMSO and TGFB1 treated primary microglia activated by LPS, respectively. The tables contain expression values of genes for the samples that were compared along with mean expression values for all samples combined, log fold change between sample groups, and adjusted p-values. in the RNA-Seq differential expression analysis of control and LPS activated primary microglia, DMSO and CX-5461 treated primary microglia activated by LPS, and DMSO and TGFB1 treated primary microglia activated by LPS, respectively.

Table S4 | Differential expression analysis of control and *Tgfb1* cKO hippocampal microglia. The table contains expression values of genes for the samples that were compared along with mean expression values for all samples combined, log fold change between sample groups, and adjusted p-values.

REFERENCES

1 Waisman, A., Ginhoux, F., Greter, M. & Bruttger, J. Homeostasis of Microglia in the Adult Brain: Review of Novel Microglia Depletion Systems. *Trends in immunology* **36**, 625-636, doi:10.1016/j.it.2015.08.005 (2015).

2 Salter, M. W. & Beggs, S. Sublime microglia: expanding roles for the guardians of the CNS. *Cell* **158**, 15-24, doi:10.1016/j.cell.2014.06.008 (2014).

3 Mosher, K. I. & Wyss-Coray, T. Microglial dysfunction in brain aging and Alzheimer's disease. *Biochem Pharmacol* **88**, 594-604, doi:10.1016/j.bcp.2014.01.008 (2014).

4 Bachiller, S. *et al.* Microglia in Neurological Diseases: A Road Map to Brain-Disease Dependent-Inflammatory Response. *Front Cell Neurosci* **12**, 488, doi:10.3389/fncel.2018.00488 (2018).

5 Sierra, A., Gottfried-Blackmore, A. C., McEwen, B. S. & Bulloch, K. Microglia derived from aging mice exhibit an altered inflammatory profile. *Glia* **55**, 412-424, doi:10.1002/glia.20468 (2007).

6 Marschallinger, J. *et al.* Lipid-droplet-accumulating microglia represent a dysfunctional and proinflammatory state in the aging brain. *Nature neuroscience* **23**, 194-208, doi:10.1038/s41593-019-0566-1 (2020).

7 Pluvinage, J. V. *et al.* CD22 blockade restores homeostatic microglial phagocytosis in ageing brains. *Nature*, doi:10.1038/s41586-019-1088-4 (2019).

8 Damani, M. R. *et al.* Age-related alterations in the dynamic behavior of microglia. *Aging Cell* **10**, 263-276, doi:10.1111/j.1474-9726.2010.00660.x (2011).

9 Flanary, B. E., Sammons, N. W., Nguyen, C., Walker, D. & Streit, W. J. Evidence that aging and amyloid promote microglial cell senescence. *Rejuvenation Res* **10**, 61-74, doi:10.1089/rej.2006.9096 (2007).

10 Udeochu, J. C., Shea, J. M. & Villeda, S. A. Microglia communication: Parallels between aging and Alzheimer's disease. *Clin Exp Neuroimmunol* **7**, 114-125, doi:10.1111/cen3.12307 (2016).

11 Grabert, K. *et al.* Microglial brain region-dependent diversity and selective regional sensitivities to aging. *Nature neuroscience* **19**, 504-516, doi:10.1038/nn.4222 (2016).

12 Burns, J. C. *et al.* Differential accumulation of storage bodies with aging defines discrete subsets of microglia in the healthy brain. *Elife* **9**, doi:10.7554/eLife.57495 (2020).

13 Hammond, T. R. *et al.* Single-Cell RNA Sequencing of Microglia throughout the Mouse Lifespan and in the Injured Brain Reveals Complex Cell-State Changes. *Immunity* **50**, 253-271 e256, doi:10.1016/j.immuni.2018.11.004 (2019).

14 Li, X. *et al.* Transcriptional and epigenetic decoding of the microglial aging process. *Nat Aging* **3**, 1288-1311, doi:10.1038/s43587-023-00479-x (2023).

1407 15 Silvin, A. *et al.* Dual ontogeny of disease-associated microglia and disease inflammatory
1408 macrophages in aging and neurodegeneration. *Immunity* **55**, 1448-1465 e1446,
1409 doi:10.1016/j.immuni.2022.07.004 (2022).

1410 16 Keren-Shaul, H. *et al.* A Unique Microglia Type Associated with Restricting Development
1411 of Alzheimer's Disease. *Cell* **169**, 1276-1290 e1217, doi:10.1016/j.cell.2017.05.018
1412 (2017).

1413 17 Sala Frigerio, C. *et al.* The Major Risk Factors for Alzheimer's Disease: Age, Sex, and
1414 Genes Modulate the Microglia Response to Abeta Plaques. *Cell Rep* **27**, 1293-1306
1415 e1296, doi:10.1016/j.celrep.2019.03.099 (2019).

1416 18 Lee, S. *et al.* APOE modulates microglial immunometabolism in response to age, amyloid
1417 pathology, and inflammatory challenge. *Cell Rep* **42**, 112196,
1418 doi:10.1016/j.celrep.2023.112196 (2023).

1419 19 Masuda, T. *et al.* Spatial and temporal heterogeneity of mouse and human microglia at
1420 single-cell resolution. *Nature* **566**, 388-392, doi:10.1038/s41586-019-0924-x (2019).

1421 20 Kaya, T. *et al.* CD8(+) T cells induce interferon-responsive oligodendrocytes and microglia
1422 in white matter aging. *Nature neuroscience* **25**, 1446-1457, doi:10.1038/s41593-022-
1423 01183-6 (2022).

1424 21 Yousef, H. *et al.* Aged blood impairs hippocampal neural precursor activity and activates
1425 microglia via brain endothelial cell VCAM1. *Nat Med* **25**, 988-1000, doi:10.1038/s41591-
1426 019-0440-4 (2019).

1427 22 Rebo, J. *et al.* A single heterochronic blood exchange reveals rapid inhibition of multiple
1428 tissues by old blood. *Nat Commun* **7**, 13363, doi:10.1038/ncomms13363 (2016).

1429 23 Villeda, S. A. *et al.* The ageing systemic milieu negatively regulates neurogenesis and
1430 cognitive function. *Nature* **477**, 90-94, doi:10.1038/nature10357 (2011).

1431 24 Li, Q. *et al.* Developmental Heterogeneity of Microglia and Brain Myeloid Cells Revealed
1432 by Deep Single-Cell RNA Sequencing. *Neuron* **101**, 207-223 e210,
1433 doi:10.1016/j.neuron.2018.12.006 (2019).

1434 25 Kracht, L. *et al.* Human fetal microglia acquire homeostatic immune-sensing properties
1435 early in development. *Science (New York, N.Y.)* **369**, 530-537,
1436 doi:10.1126/science.aba5906 (2020).

1437 26 Fan, X., Wheatley, E. G. & Villeda, S. A. Mechanisms of Hippocampal Aging and the
1438 Potential for Rejuvenation. *Annu Rev Neurosci* **40**, 251-272, doi:10.1146/annurev-neuro-
1439 072116-031357 (2017).

1440 27 Millet, A., Ledo, J. H. & Tavazoie, S. F. An exhausted-like microglial population
1441 accumulates in aged and APOE4 genotype Alzheimer's brains. *Immunity* **57**, 153-170
1442 e156, doi:10.1016/j.immuni.2023.12.001 (2024).

1443 28 Harrington, E. P. *et al.* MHC class I and MHC class II reporter mice enable analysis of
1444 immune oligodendroglia in mouse models of multiple sclerosis. *Elife* **12**,
1445 doi:10.7554/eLife.82938 (2023).

1446 29 Shi, Q. *et al.* Complement C3-Deficient Mice Fail to Display Age-Related Hippocampal
1447 Decline. *J Neurosci* **35**, 13029-13042, doi:10.1523/jneurosci.1698-15.2015 (2015).

1448 30 Kozareva, D. A., Cryan, J. F. & Nolan, Y. M. Born this way: Hippocampal neurogenesis
1449 across the lifespan. *Aging Cell* **18**, e13007, doi:10.1111/acel.13007 (2019).

1450 31 Seki, T. & Arai, Y. Age-related production of new granule cells in the adult dentate gyrus.
1451 *Neuroreport* **6**, 2479-2482, doi:10.1097/00001756-199512150-00010 (1995).

1452 32 Taniguchi, K. & Karin, M. NF-kappaB, inflammation, immunity and cancer: coming of age.
1453 *Nat Rev Immunol* **18**, 309-324, doi:10.1038/nri.2017.142 (2018).

1454 33 Butovsky, O. *et al.* Identification of a unique TGF-beta-dependent molecular and functional
1455 signature in microglia. *Nature neuroscience* **17**, 131-143, doi:10.1038/nn.3599 (2014).

1456 34 Bedolla, A. *et al.* Adult microglial TGFbeta1 is required for microglia homeostasis via an
1457 autocrine mechanism to maintain cognitive function in mice. *Nat Commun* **15**, 5306,
1458 doi:10.1038/s41467-024-49596-0 (2024).

1459 35 Bieri, G., Schroer, A. B. & Villeda, S. A. Blood-to-brain communication in aging and
1460 rejuvenation. *Nature neuroscience* **26**, 379-393, doi:10.1038/s41593-022-01238-8 (2023).

1461 36 Ransohoff, R. M. How neuroinflammation contributes to neurodegeneration. *Science*
1462 *(New York, N.Y.)* **353**, 777-783, doi:10.1126/science.aag2590 (2016).

1463 37 Pálovics, R. *et al.* Molecular hallmarks of heterochronic parabiosis at single-cell resolution.
1464 *Nature* **603**, 309-314, doi:10.1038/s41586-022-04461-2 (2022).

1465 38 Palovics, R. *et al.* Molecular hallmarks of heterochronic parabiosis at single-cell resolution.
1466 *Nature* **603**, 309-314, doi:10.1038/s41586-022-04461-2 (2022).

1467 39 Yi, Y. W., You, K. S., Park, J. S., Lee, S. G. & Seong, Y. S. Ribosomal Protein S6: A
1468 Potential Therapeutic Target against Cancer? *Int J Mol Sci* **23**, doi:10.3390/ijms23010048
1469 (2021).

1470 40 Spittau, B., Dokalis, N. & Prinz, M. The Role of TGFbeta Signaling in Microglia Maturation
1471 and Activation. *Trends in immunology* **41**, 836-848, doi:10.1016/j.it.2020.07.003 (2020).

1472 41 Cserép, C., Pósfai, B. & Dénes, Á. Shaping Neuronal Fate: Functional Heterogeneity of
1473 Direct Microglia-Neuron Interactions. *Neuron* **109**, 222-240,
1474 doi:10.1016/j.neuron.2020.11.007 (2021).

1475 42 Horowitz, A. M. *et al.* Blood factors transfer beneficial effects of exercise on neurogenesis
1476 and cognition to the aged brain. *Science (New York, N.Y.)* **369**, 167-173,
1477 doi:10.1126/science.aaw2622 (2020).

1478 43 Traschütz, A., Kummer, M. P., Schwartz, S. & Heneka, M. T. Variability and temporal
1479 dynamics of novel object recognition in aging male C57BL/6 mice. *Behav Processes* **157**,
1480 711-716, doi:10.1016/j.beproc.2017.11.009 (2018).

1481 44 Phillips, R. G. & LeDoux, J. E. Differential contribution of amygdala and hippocampus to
1482 cued and contextual fear conditioning. *Behav Neurosci* **106**, 274-285, doi:10.1037//0735-
1483 7044.106.2.274 (1992).

1484 45 Kraeuter, A. K., Guest, P. C. & Sarnyai, Z. The Y-Maze for Assessment of Spatial Working
1485 and Reference Memory in Mice. *Methods Mol Biol* **1916**, 105-111, doi:10.1007/978-1-
1486 4939-8994-2_10 (2019).

1487 46 Kaiser, T. & Feng, G. Tmem119-EGFP and Tmem119-CreERT2 Transgenic Mice for
1488 Labeling and Manipulating Microglia. *eNeuro* **6**, doi:10.1523/ENEURO.0448-18.2019
1489 (2019).

1490 47 Wek, R. C. Role of eIF2alpha Kinases in Translational Control and Adaptation to Cellular
1491 Stress. *Cold Spring Harb Perspect Biol* **10**, doi:10.1101/cshperspect.a032870 (2018).

1492 48 Lopez-Otin, C., Blasco, M. A., Partridge, L., Serrano, M. & Kroemer, G. The hallmarks of
1493 aging. *Cell* **153**, 1194-1217, doi:10.1016/j.cell.2013.05.039 (2013).

1494 49 Chovatiya, R. & Medzhitov, R. Stress, inflammation, and defense of homeostasis. *Mol Cell*
1495 **54**, 281-288, doi:10.1016/j.molcel.2014.03.030 (2014).

1496 50 Xu, Z. X. *et al.* Elevated protein synthesis in microglia causes autism-like synaptic and
1497 behavioral aberrations. *Nat Commun* **11**, 1797, doi:10.1038/s41467-020-15530-3 (2020).

1498 51 Yin, Z. *et al.* APOE4 impairs the microglial response in Alzheimer's disease by inducing
1499 TGFbeta-mediated checkpoints. *Nat Immunol* **24**, 1839-1853, doi:10.1038/s41590-023-
1500 01627-6 (2023).

1501 52 Sarlus, H. & Heneka, M. T. Microglia in Alzheimer's disease. *J Clin Invest* **127**, 3240-3249,
1502 doi:10.1172/JCI90606 (2017).

1503 53 Smith, L. K. *et al.* beta2-microglobulin is a systemic pro-aging factor that impairs cognitive
1504 function and neurogenesis. *Nat Med* **21**, 932-937, doi:10.1038/nm.3898 (2015).

1505 54 Trombetta, J. J. *et al.* Preparation of Single-Cell RNA-Seq Libraries for Next Generation
1506 Sequencing. *Curr Protoc Mol Biol* **107**, 4 22 21-17, doi:10.1002/0471142727.mb0422s107
1507 (2014).

1508 55 Bray, N. L., Pimentel, H., Melsted, P. & Pachter, L. Near-optimal probabilistic RNA-seq
1509 quantification. *Nat Biotechnol* **34**, 525-527, doi:10.1038/nbt.3519 (2016).

1510 56 Love, M. I., Huber, W. & Anders, S. Moderated estimation of fold change and dispersion
1511 for RNA-seq data with DESeq2. *Genome Biol* **15**, 550, doi:10.1186/s13059-014-0550-8
1512 (2014).

1513 57 Ashburner, M. *et al.* Gene ontology: tool for the unification of biology. The Gene Ontology
1514 Consortium. *Nat Genet* **25**, 25-29, doi:10.1038/75556 (2000).

58 Gene Ontology, C. The Gene Ontology resource: enriching a GOld mine. *Nucleic Acids Res* **49**, D325-D334, doi:10.1093/nar/gkaa1113 (2021).

59 Mi, H., Muruganujan, A., Ebert, D., Huang, X. & Thomas, P. D. PANTHER version 14: more genomes, a new PANTHER GO-slim and improvements in enrichment analysis tools. *Nucleic Acids Res* **47**, D419-D426, doi:10.1093/nar/gky1038 (2019).

60 Zheng, G. X. *et al.* Massively parallel digital transcriptional profiling of single cells. *Nat Commun* **8**, 14049, doi:10.1038/ncomms14049 (2017).

61 Marsh, S. E. *et al.* Dissection of artifactual and confounding glial signatures by single-cell sequencing of mouse and human brain. *Nat Neurosci* **25**, 306-316, doi:10.1038/s41593-022-01022-8 (2022).

62 Butler, A., Hoffman, P., Smibert, P., Papalexi, E. & Satija, R. Integrating single-cell transcriptomic data across different conditions, technologies, and species. *Nat Biotechnol* **36**, 411-420, doi:10.1038/nbt.4096 (2018).

63 Qiu, X. *et al.* Single-cell mRNA quantification and differential analysis with Census. *Nat Methods* **14**, 309-315, doi:10.1038/nmeth.4150 (2017).

64 Qiu, X. *et al.* Reversed graph embedding resolves complex single-cell trajectories. *Nat Methods* **14**, 979-982, doi:10.1038/nmeth.4402 (2017).

65 Trapnell, C. *et al.* The dynamics and regulators of cell fate decisions are revealed by pseudotemporal ordering of single cells. *Nat Biotechnol* **32**, 381-386, doi:10.1038/nbt.2859 (2014).

66 Cao, J. *et al.* The single-cell transcriptional landscape of mammalian organogenesis. *Nature* **566**, 496-502, doi:10.1038/s41586-019-0969-x (2019).

67 Saelens, W., Cannoodt, R., Todorov, H. & Saeys, Y. A comparison of single-cell trajectory inference methods. *Nat Biotechnol* **37**, 547-554, doi:10.1038/s41587-019-0071-9 (2019).

68 Leger, M. *et al.* Object recognition test in mice. *Nat Protoc* **8**, 2531-2537, doi:10.1038/nprot.2013.155 (2013).

69 Belarbi, K. *et al.* Beneficial effects of exercise in a transgenic mouse model of Alzheimer's disease-like Tau pathology. *Neurobiol Dis* **43**, 486-494, doi:10.1016/j.nbd.2011.04.022 (2011).

70 Pasciuto, E. *et al.* Microglia Require CD4 T Cells to Complete the Fetal-to-Adult Transition. *Cell* **182**, 625-640 e624, doi:10.1016/j.cell.2020.06.026 (2020).

71 Qin, Y. *et al.* A Milieu Molecule for TGF-beta Required for Microglia Function in the Nervous System. *Cell* **174**, 156-171 e116, doi:10.1016/j.cell.2018.05.027 (2018).

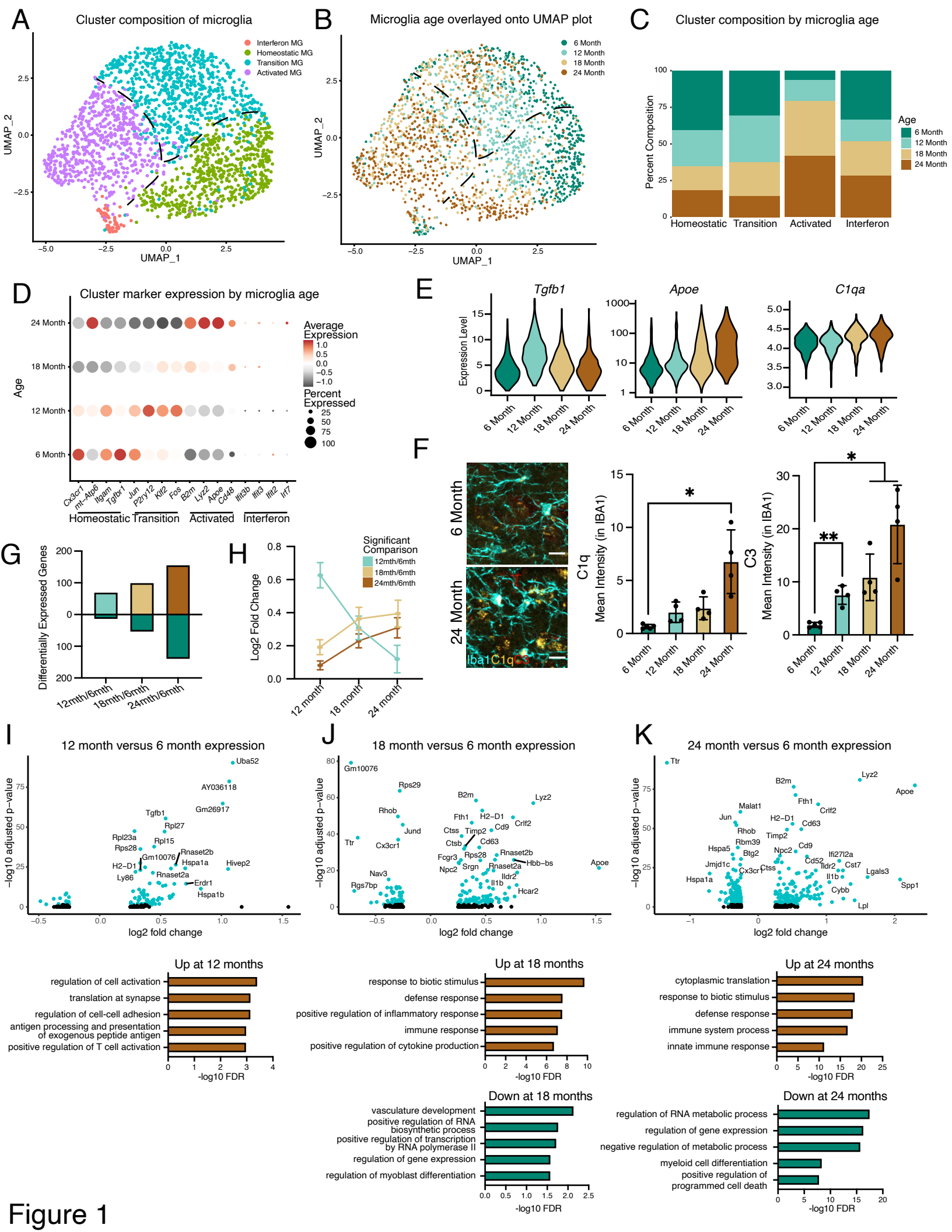
A
Cluster composition of microglia
Interferon MG
Homeostatic MG
Transition MG
Activated MG
UMAP_2
UMAP_1
B
Microglia age overlayed onto UMAP plot
6 Month
12 Month
18 Month
24 Month
C
Cluster composition by microglia age
Percent Composition
Homeostatic
Transition
Activated
Interferon
Age
D
Cluster marker expression by microglia age
Average Expression
Percent Expressed
Age
Cx3cr1
mt-Atp6
Itgam
Tgfbr1
Jun
P2ry12
Klf2
Fos
B2m
Lyz2
Apoe
Cd48
Ifit3b
Ifit3
Ifit2
Irf7
Homeostatic
Transition
Activated
Interferon
E
Tgfb1
Apoe
C1qa
Expression Level
F
6 Month
24 Month
Iba1C1qC3
C1q
C3
Mean Intensity (in IBA1)
G
Differentially Expressed Genes
12mth/6mth
18mth/6mth
24mth/6mth
H
Log2 Fold Change
Significant Comparison
12mth/6mth
18mth/6mth
24mth/6mth
I
12 month versus 6 month expression
J
18 month versus 6 month expression
K
24 month versus 6 month expression
−log10 adjusted p−value
log2 fold change
Up at 12 months
regulation of cell activation
translation at synapse
regulation of cell-cell adhesion
antigen processing and presentation of exogenous peptide antigen
positive regulation of T cell activation
Up at 18 months
response to biotic stimulus
defense response
positive regulation of inflammatory response
immune response
positive regulation of cytokine production
Up at 24 months
cytoplasmic translation
response to biotic stimulus
defense response
immune system process
innate immune response
Down at 18 months
vasculature development
positive regulation of RNA biosynthetic process
positive regulation of transcription by RNA polymerase II
regulation of gene expression
regulation of myoblast differentiation
Down at 24 months
regulation of RNA metabolic process
regulation of gene expression
negative regulation of metabolic process
myeloid cell differentiation
positive regulation of programmed cell death
-log10 FDR

Figure 1

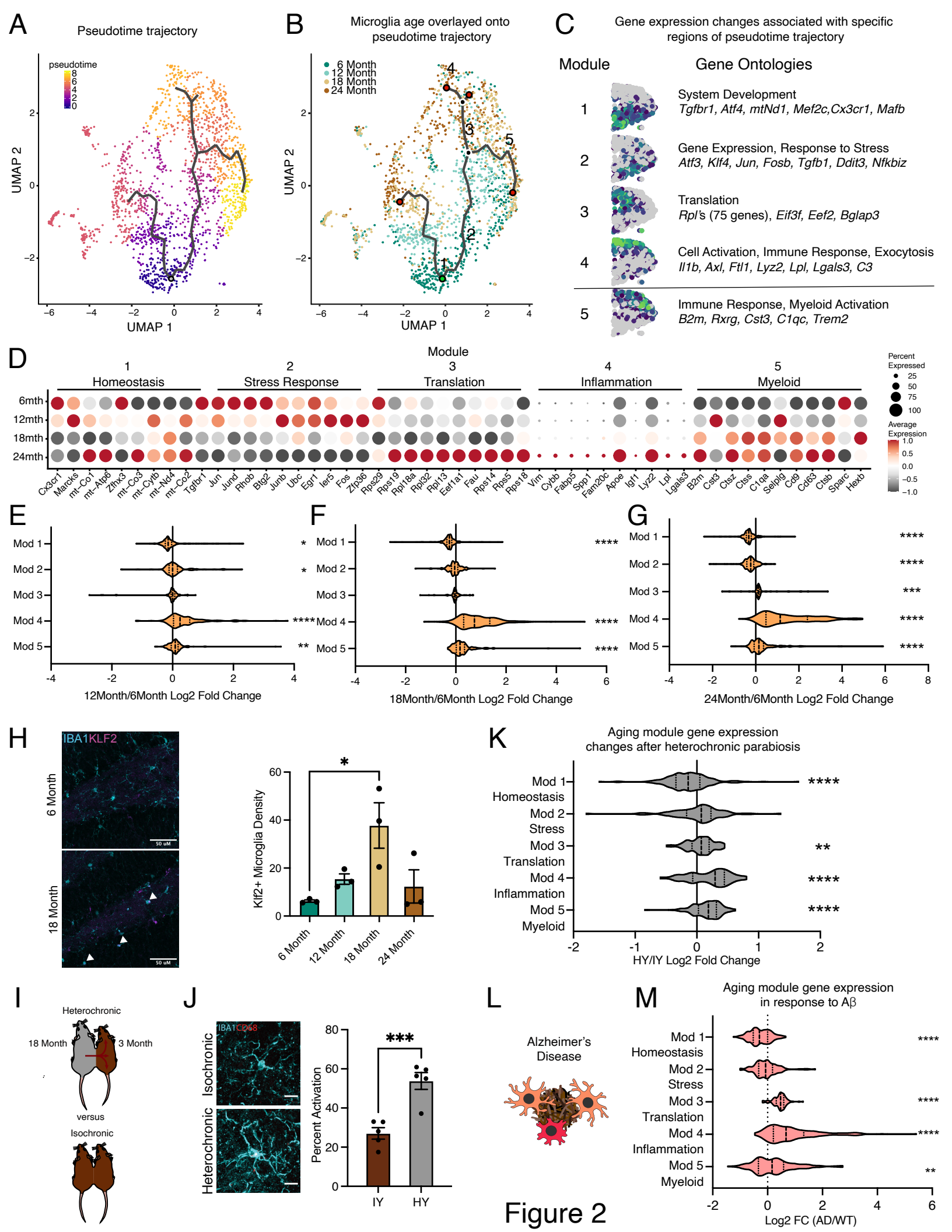
A
Pseudotime trajectory
pseudotime
UMAP 1
UMAP 2
B
Microglia age overlayed onto pseudotime trajectory
6 Month
12 Month
18 Month
24 Month
C
Gene expression changes associated with specific regions of pseudotime trajectory
Module
Gene Ontologies
1 System Development
Tgfbr1, Atf4, mtNd1, Mef2c,Cx3cr1, Mafb
2 Gene Expression, Response to Stress
Atf3, Klf4, Jun, Fosb, Tgfb1, Ddit3, Nfkbiz
3 Translation
Rpl's (75 genes), Eif3f, Eef2, Bglap3
4 Cell Activation, Immune Response, Exocytosis
Il1b, Axl, Ftl1, Lyz2, Lpl, Lgals3, C3
5 Immune Response, Myeloid Activation
B2m, Rxrg, Cst3, C1qc, Trem2
D
Module
1 Homeostasis
2 Stress Response
3 Translation
4 Inflammation
5 Myeloid
6mth
12mth
18mth
24mth
Percent Expressed
Average Expression
E
12Month/6Month Log2 Fold Change
F
18Month/6Month Log2 Fold Change
G
24Month/6Month Log2 Fold Change
Mod 1
Mod 2
Mod 3
Mod 4
Mod 5
H
IBA1KLF2
6 Month
18 Month
Klf2+ Microglia Density
I
Heterochronic
18 Month
3 Month
versus
Isochronic
J
IBA1CD68
Isochronic
Heterochronic
Percent Activation
IY
HY
K
Aging module gene expression changes after heterochronic parabiosis
Mod 1 Homeostasis
Mod 2 Stress
Mod 3 Translation
Mod 4 Inflammation
Mod 5 Myeloid
HY/IY Log2 Fold Change
L
Alzheimer's Disease
M
Aging module gene expression in response to Aβ
Log2 FC (AD/WT)

Figure 2

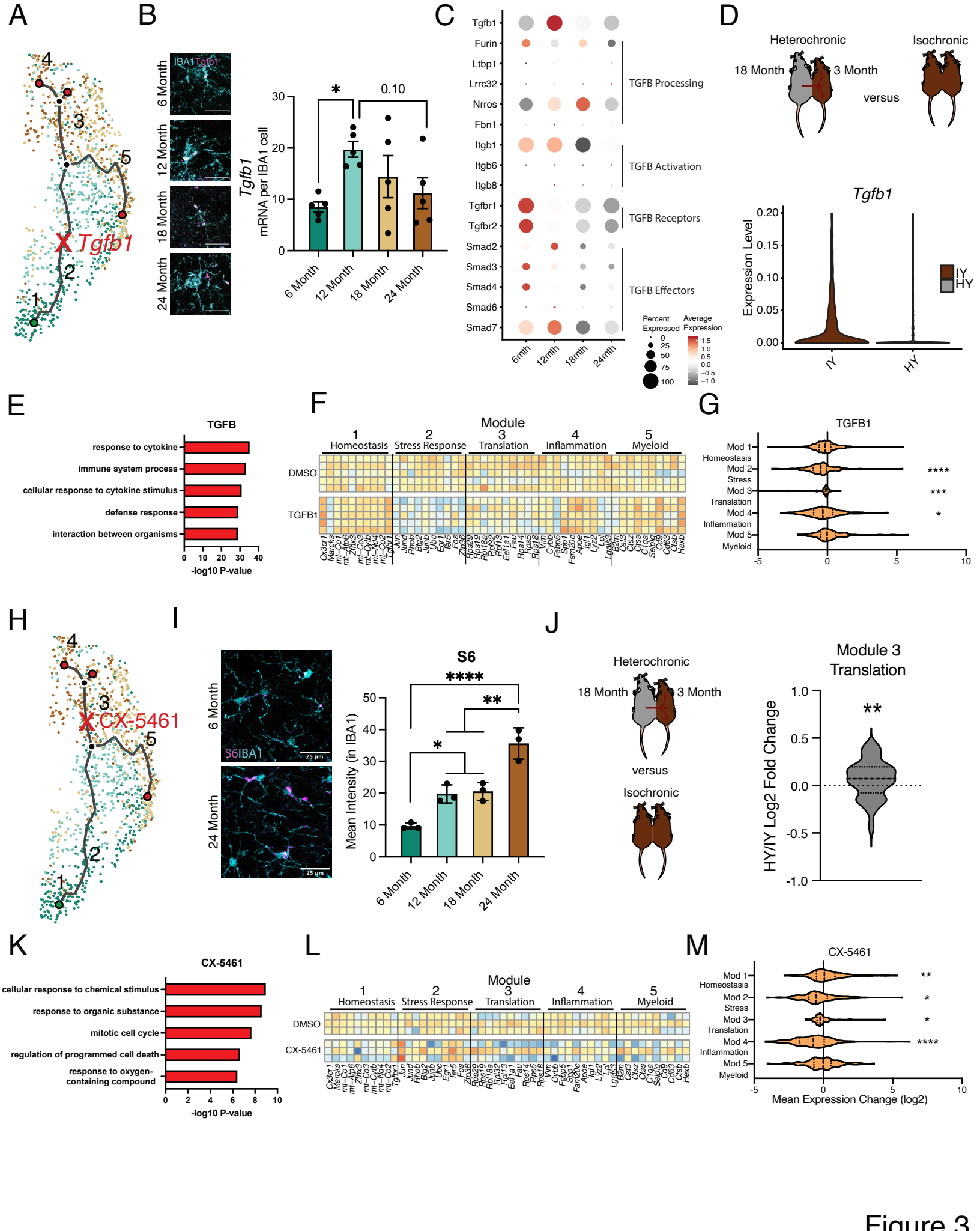
A
4
3
5
Tgfb1
2
1
B
IBA1Tgfb1
6 Month
12 Month
18 Month
24 Month
Tgfb1
mRNA per IBA1 cell
*
0.10
C
Tgfb1
Furin
Ltbp1
Lrrc32
Nrros
Fbn1
Itgb1
Itgb6
Itgb8
Tgfbr1
Tgfbr2
Smad2
Smad3
Smad4
Smad6
Smad7
TGFB Processing
TGFB Activation
TGFB Receptors
TGFB Effectors
6mth
12mth
18mth
24mth
Percent Expressed
Average Expression
D
Heterochronic
Isochronic
18 Month
3 Month
versus
Tgfb1
Expression Level
IY
HY
E
TGFB
response to cytokine
immune system process
cellular response to cytokine stimulus
defense response
interaction between organisms
-log10 P-value
F
Module
1 Homeostasis
2 Stress Response
3 Translation
4 Inflammation
5 Myeloid
DMSO
TGFB1
G
TGFB1
Mod 1
Homeostasis
Mod 2
Stress
Mod 3
Translation
Mod 4
Inflammation
Mod 5
Myeloid
H
4
3
CX-5461
5
2
1
I
6 Month
24 Month
S6IBA1
25 µm
S6
Mean Intensity (in IBA1)
****
**
*
J
Heterochronic
18 Month
3 Month
versus
Isochronic
Module 3
Translation
HY/IY Log2 Fold Change
K
CX-5461
cellular response to chemical stimulus
response to organic substance
mitotic cell cycle
regulation of programmed cell death
response to oxygen-containing compound
-log10 P-value
L
Module
1 Homeostasis
2 Stress Response
3 Translation
4 Inflammation
5 Myeloid
DMSO
CX-5461
M
CX-5461
Mod 1
Homeostasis
Mod 2
Stress
Mod 3
Translation
Mod 4
Inflammation
Mod 5
Myeloid
Mean Expression Change (log2)

Figure 3

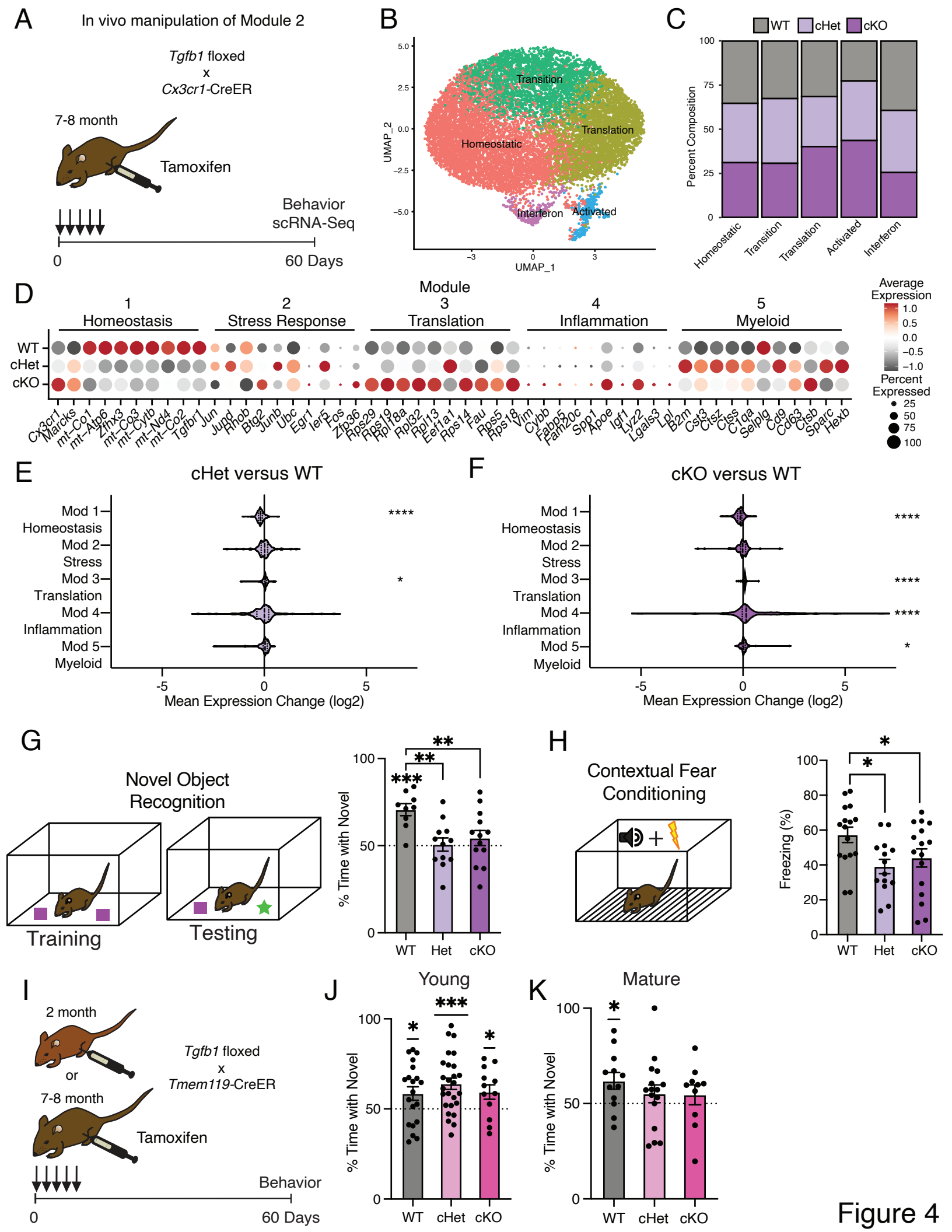
A
In vivo manipulation of Module 2
Tgfb1 floxed
x
Cx3cr1-CreER
7-8 month
Tamoxifen
Behavior
scRNA-Seq
0
60 Days
B
Transition
Translation
Homeostatic
Interferon
Activated
UMAP_2
UMAP_1
C
WT
cHet
cKO
Percent Composition
Homeostatic
Transition
Translation
Activated
Interferon
D
Module
1 Homeostasis
2 Stress Response
3 Translation
4 Inflammation
5 Myeloid
WT
cHet
cKO
Average Expression
Percent Expressed
Cx3cr1 Marcks mt-Co1 mt-Atp6 Zfhx3 mt-Co3 mt-Cytb mt-Nd4 mt-Co2 Tgfbr1 Jun Jund Rhob Btg2 Junb Ubc Egr1 Ier5 Fos Zfp36 Rps29 Rps19 Rpl18a Rpl32 Rpl13 Eef1a1 Rps14 Fau Rps5 Rps18 Vim Cybb Fabp5 Fam20c Spp1 Apoe Igf1 Lyz2 Lgals3 Lpl B2m Cst3 Ctsz Ctss C1qa Selplg Cd9 Cd63 Ctsb Sparc Hexb
E
cHet versus WT
Mod 1 Homeostasis
Mod 2 Stress
Mod 3 Translation
Mod 4 Inflammation
Mod 5 Myeloid
Mean Expression Change (log2)
F
cKO versus WT
Mean Expression Change (log2)
G
Novel Object Recognition
Training
Testing
% Time with Novel
WT
Het
cKO
H
Contextual Fear Conditioning
Freezing (%)
WT
Het
cKO
I
2 month
or
7-8 month
Tgfb1 floxed
x
Tmem119-CreER
Tamoxifen
Behavior
0
60 Days
J
Young
% Time with Novel
WT
cHet
cKO
K
Mature
% Time with Novel
WT
cHet
cKO

Figure 4